BridgeR: A Regional Seismic Hazard Assessment Framework for Transportation Networks and Its Application to Freight Loss Assessment

October 2022

A Research from the Pacific Southwest Region University Transportation Center

Barbaros Cetiner, University of California, Berkeley

Ertugrul Taciroglu, University of California, Los Angeles

Pacific Southwest Region UTC

University Transportation Center

TECHNICAL REPORT DOCUMENTATION PAGE

1. Report No.	2. Government Accession No.	3. Recipient's Catalog No.
PSR-17-05	N/A	N/A

4. Title and Subtitle BridgeR: A Regional Seismic Hazard Assessment Framework for Transportation Networks and Its Application to Freight Loss Assessment	**5. Report Date** 10/31/2022 **6. Performing Organization Code** N/A
7. Author(s) Barbaros Cetiner, 0000-0002-9726-8120 Ertugrul Taciroglu, 0000-0001-9618-1210	**8. Performing Organization Report No.** TBD
9. Performing Organization Name and Address METRANS Transportation Center University of Southern California University Park Campus, RGL 216 Los Angeles, CA 90089-0626	**10. Work Unit No.** N/A **11. Contract or Grant No.** USDOT Grant 69A3551747109
12. Sponsoring Agency Name and Address U.S. Department of Transportation Office of the Assistant Secretary for Research and Technology 1200 New Jersey Avenue, SE, Washington, DC 20590	**13. Type of Report and Period Covered** Final report (11/1/2019 to 10/31/2020) **14. Sponsoring Agency Code** USDOT OST-R

15. Supplementary Notes
Some products of this research are made available to the general public on the project website http://shakeready.org/

16. Abstract
This project aims to establish a new engineering workflow that enables high-fidelity assessment of the impacts of seismic hazards on bridge infrastructure and the resulting disruptions to the traffic flow on transportation networks. The traditional approaches to quantifying the vulnerability of transportation networks to natural hazards involve many mathematical simplifications, both in predicting the physical damage to transportation infrastructure and simulating the resulting traffic disruptions. The devised workflow overcomes these issues by implementing a state-of-the-art image-based bridge modeling methodology and coupling the physical damage predictions of these models with agent-based transportation models to evaluate the effects of natural hazards on transportation networks at a level that has not yet been achieved. A demonstrative use case of BridgeR on Ports of Los Angeles and Long Beach Area freight traffic provides critical insights into BridgeR's ability to identify potential vulnerabilities of transportation networks. Preliminary findings of this study for a realistic large-magnitude seismic event indicate impacts to almost half of the daily freight trips to and from the Ports of Los Angeles and Long Beach, which may result in indirect economic consequences of over 100 million USD.

17. Key Words Natural Hazards Engineering, Transportation Networks, Resilience, Computer Vision, Traffic Simulation, Case Studies	**18. Distribution Statement** No restrictions.

19. Security Classif. (of this report)	20. Security Classif. (of this page)	21. No. of Pages	22. Price
Unclassified	Unclassified	66	N/A

Form DOT F 1700.7 (8-72) Reproduction of completed page authorized

Pacific Southwest Region UTC
University Transportation Center

Contents

About the Pacific Southwest Region University Transportation Center

The Pacific Southwest Region University Transportation Center (UTC) is the Region 9 University Transportation Center funded under the US Department of Transportation's University Transportation Centers Program. Established in 2016, the Pacific Southwest Region UTC (PSR) is led by the University of Southern California and includes seven partners: Long Beach State University; University of California, Davis; University of California, Irvine; University of California, Los Angeles; University of Hawaii; Northern Arizona University; Pima Community College.

The Pacific Southwest Region UTC conducts an integrated, multidisciplinary program of research, education and technology transfer aimed at *improving the mobility of people and goods throughout the region.* Our program is organized around four themes: 1) technology to address transportation problems and improve mobility; 2) improving mobility for vulnerable populations; 3) Improving resilience and protecting the environment; and 4) managing mobility in high growth areas.

U.S. Department of Transportation (USDOT) Disclaimer

California Department of Transportation (CALTRANS) Disclaimer

Disclosure

Principal Investigator, Co-Principal Investigators, others, conducted this research titled, "BridgeR: A Regional Seismic Hazard Assessment Tool for Transportation Networks and Its Application to Freight Loss Assessment" at University of California, Los Angeles. The research took place from 11/1/2019 to 10/31/2020 and was funded by a grant from the UC Institute of Transportations Studies in the amount of $105,000. The research was conducted as part of the Pacific Southwest Region University Transportation Center research program.

Acknowledgements

Authors acknowledge the assistance provided by Professor Brian Taylor (UCLA) and Dr. Juan Matute (UCLA) as well as collaborators Mr. Michael Virtucio, Dr. Bingyu Zhao, and Professor Kenichi Soga (UC Berkeley) who helped carry out the traffic analyses presented in this report.

Abstract

This project aims to establish a new engineering workflow that enables high-fidelity assessment of the impacts of seismic hazards on bridge infrastructure and the resulting disruptions to the traffic flow on transportation networks. The traditional approaches to quantifying the vulnerability of transportation networks to natural hazards involve many mathematical simplifications, both in terms of predicting the physical damage to transportation infrastructure and simulating the resulting traffic disruptions. BridgeR workflow overcomes these issues by implementing a state-of-the-art image-based bridge modeling methodology and coupling the physical damage predictions of these models with agent-based transportation models to evaluate the effects of natural hazards on transportation networks at a level that has not yet been achieved. A demonstrative use case of BridgeR on Ports of Los Angeles and Long Beach Area freight traffic provides critical insights into BridgeR's ability to identify potential vulnerabilities of transportation networks. Preliminary findings of this study for a realistic large-magnitude seismic event indicate impacts to almost half of the daily freight trips to and from the Ports of Los Angeles and Long Beach, which may result in indirect economic consequences of over 100 million USD.

BridgeR: A Regional Seismic Hazard Assessment Workflow for Transportation Networks and Its Application to Freight Loss Assessment

Executive Summary

The civil infrastructure is aging at a rate that outpaces the maintenance and rehabilitation efforts, routinely requiring the use of civil structures and facilities past their designated service life. The complications associated with the overutilization of civil infrastructure are further compounded by the latest developments in hazards engineering indicating that some previous design practices may result in critical vulnerabilities to natural hazards. These weaknesses must be identified and addressed to limit devastation from natural hazards. With the funds required to meet the retrofitting needs of infrastructure components being so limited and our understanding of the complex interactions within the individual elements of civil infrastructure so scarce, effectively allocating the resources to contain the potential impacts of natural hazards is a daunting task. Traditional methods of predicting the post-disaster performance of civil infrastructure fall short of modeling the complexities of these distributed systems. This study provides a state-of-the-art workflow, BridgeR, for evaluating the post-disaster performance of the transportation infrastructure, assuming bridge structures as the primary driver of the post-disaster performance.

Unlike the traditional loss assessment methods for Transportation Networks, BridgeR computes the physical damage to bridges using a bridge-specific approach and couples these physical damage predictions with the network-level behavior to quantify the disaster impact in dollars, traffic delays, and additional miles traveled for an entire region. The physical damage prediction component of BridgeR uses an automated image-based Bridge Modeling module explicitly developed for the BridgeR workflow. To obtain the imagery required for establishing the geometric bridge models, the Bridge Modeling module receives bridge locations from the National Bridge Inventory (NBI), extracts the centerline geometry of each bridge corresponding to its NBI seed using OpenStreetMap (OSM) data via geometric and route information search and downloads the bridge imagery along this determined centerline geometry. Then the module runs the images collected for each bridge through a structure-from-motion algorithm to convert the image data into a point cloud. This point cloud is then segmented by mapping the segmentation masks from street-level imagery to the point cloud data to determine deck, column, in-span hinge, and abutment geometric dimensions. The segmentation model used for this purpose uses the DeepLabv3 architecture. Abutment and bent type classifiers used to identify the substructure type for each bridge use the EfficientNetv2-M architecture. Both models were trained on images custom labeled by the Taciroglu Research Group. Collectively, these components of the Bridge Modeling module generate detailed 3D geometric models of bridges in an automated manner. The Bridge Modeling module populates these 3D models with structural properties by using the class statistics available in the literature, for properties ranging from typical reinforcement ratios to foundation spring stiffness coefficients, to create individual OpenSees models, and

subsequently fragility functions. These fragility functions when combined with the output from the hazard calculation component of BridgeR enable probabilistic determination of expected physical damages to bridges (i.e., bridge losses).

The traffic simulation component of BridgeR ingests the physical losses and converts this information to network links that are removed or operated at a reduced capacity based on the severity of the losses. To capture the effects of bridge damage on the traffic network performance at a large geographic scale, BridgeR uses an open-sourced agent-based semi-dynamic traffic assignment model. The base road network information is extracted from OSM, and various traffic-related attributes are assigned to the road links, including length, speed limit, and capacity, based on the OSM attributes. Traffic simulations are performed at a time step of 15 minutes in a way designed to increase the stability of the results by avoiding all vehicles getting assigned to the same routes at once. After each increment, the traffic congestion status is updated for the network. A new travel time is calculated for each link using the Bureau of Public Roads (BPR) volume-delay curves, modified to consider traffic signal, and crossing delays.

To demonstrate a practical use case of BridgeR, the potential effects of a magnitude 7.3 hypothetical earthquake 2 miles off the coast of Port of Los Angeles and Port of Long Beach (POLA, POLB) were quantified. For the purposes of quantifying the bridge damages due to this earthquake, structural models of 1,000 bridges in immediate surroundings of POLA and POLB were developed using BridgeR. Coupling this bridge damage information with a detailed transportation model of the Los Angeles area implemented using BridgeR, the disruptions to the 200,000 daily freight trips to and from POLA-POLB were analyzed. This event was found to affect Los Angeles area traffic patterns extensively. 75,000 daily freight trips were found to be severely disrupted, resulting in a total economic impact of 123 million USD just due to these impacted trips.

Introduction

Quantifying the effects of natural hazards on engineering systems has long been the focus of civil engineers. As a result of this continued attention, considerable research has been performed in developing methods to simulate the engineering demands caused by natural hazards, as well as establishing modeling techniques required for accurate representations of the capacity of civil engineering systems.

In earthquake engineering, three developments have been crucial. Probabilistic seismic hazard maps created an effective way of summarizing in detail the expected earthquake shaking based on region-specific geologic and seismic information (e.g., United States National Seismic Hazard Maps (*1*)). Comprehensive ground motion databases, such as NGA West2 Database (*2*), provided earthquake engineers with extensive catalogs of recorded seismic waveforms for use in simulating expected earthquake loading. Lastly, the performance-based earthquake engineering (PBEE) methodology (*3*) created a way to incorporate seismic hazard, system response, component-level damage, and system-level decision variables with explicit consideration to their uncertainties.

The aforementioned procedures offer means of determining the *demands* anticipated on engineering systems for seismic hazards. Demands, however, are just one of the two high-level inputs required for assessing the response of structural or geotechnical systems to natural hazards. Assessing the ability of a system to resist demands from relevant hazards requires comparing its *capacity* against the corresponding demands. Based on the complexity of the hazard input, a system's capacity is quantified through models as simple as linear elastic or as intricate as complex nonlinear representations. As long as accurate information on the system's geometric and material properties exists, appropriate models can be established, and the system capacity can be calculated with minimal uncertainty.

This process is equally applicable to evaluating the performance of individual systems or entire regions comprising a large number of distinct, but typically interacting, systems. Nonetheless, traditionally, at the level of detail specified earlier, it has been mainly utilized for single systems. On a regional scale, only simplistic implementations of the discussed principles were performed. Expectedly, as a consequence of their rather crude consideration of either the hazard, physical inventory, or both, they result in predictions far from reliable (see, for instance, the study by Kircher and co-workers (*4*)). However, in reality, the post-disaster functionality of an engineering system is remarkably dependent on the systems surrounding it. For instance, in densely urbanized areas, the seismic demands on a building can be considerably altered by the interactions of the neighboring structures with the free-field motion (*5*)—likewise, the arrangement of structures surrounding a building can largely influence the wind load demands on that building (*6*).

Most of the preceding discussion assumes that the key determinant of a system's functionality is physical damage. If functionality is perceived from a broader perspective as a system's ability to perform as intended and any reductions to it are tied to macro-level metrics such as economic losses, then shifting from the *individual* to *regional* level assessments becomes even more critical in evaluating post-disaster performance. After a natural hazard, the capability of an engineering system to restore its operations in full is linked to the infrastructure serving it.

In other words, if the objective is to determine the high-level impacts of disasters, a greater extent of interconnectedness exists between engineering systems, and this dependence can be hardly ignored. Modern-day examples supporting this understanding are countless. The annual direct cost of damage to power lines, utility poles, and transmission towers due to hurricanes or other extreme weather events is estimated at around tens to hundreds of millions of dollars (*7*). However, according to Campbell (*8*), the annual cost of power outages resulting from these physical damages is estimated somewhere between 25 to 70 billion USD. Electrical grids consist of a large number of interdependent elements. Even damage to a small fraction of their elements may result in notable reductions to functionality at the network level. As a result, considerable downstream economic losses may be incurred.

A somewhat less obvious example is how the performance of port facilities is highly reliant on the functionality of the infrastructure serving them. The property losses due to the 1995 Hanshin-Awaji (Kobe), Japan earthquake is estimated at 100 billion USD (*9*). The earthquake devastated Kobe's infrastructure in large, yet the damages to its container port (then the world's sixth-largest) were particularly critical. The business interruptions caused by the facilities' downtime and the decline in their accessibility is believed to result in total losses on the order of 200 billion USD (*10*). In the case of cargo ports, the number of goods that can be conveyed through the facilities is affected by the functionality of connecting infrastructure, and the port itself. Hence, in evaluating the effects of potential hazards to a port, if assessments of damage are limited to individual elements alone, results would have a minimal resemblance to the actual consequences.

A similar situation was observed in 2005, in the aftermath of Hurricane Katrina, one of the costliest natural disasters in the history of the United States. The total losses due to the hurricane are believed to be around 200 billion USD (*11*), while the associated property damage is approximately 96 billion USD (*12*). Katrina flooded most of New Orleans, incapacitated a remarkable portion of its infrastructure, and crippled almost the entire area. A direct result of the widespread decline in infrastructure functionality was economic losses that far exceeded the costs required to prevent these functionality decreases. For instance, after the hurricane, many of the high-rise buildings in Downtown New Orleans remained unscathed from wind and flood hazards (*13*). Still, they could not be used because the utility and transportation infrastructure that they depended on were barely operational.

In short, the post-disaster functionality of an engineering system is highly dependent on the infrastructure surrounding it. Consequently, in evaluating the potential impacts of natural hazards on a system, regional-level interactions must be considered to obtain accurate results incorporating limited uncertainty. Implementations at regional-level, nevertheless, command an added level of complexity both from the computational and modeling aspects. While the computational requirements of regional-level considerations are largely satisfied with the wide availability of web-based high-performance computing platforms—e.g., NSF's Natural Hazards Engineering Research Infrastructure (NHERI) cyberinfrastructure (*14*), Google Cloud Platform, etc.—the modeling front mostly remains in its infancy. There is a lack of dependable inventory data at the regional level. Hence, for representing capacity, the existing methods heavily rely on abstractions of the archetype system classifications based on public-domain metadata (see, for instance, HAZUS (*15*), PAGER (*16*), etc.).

Objectives of this study

The first objective of this project is to develop a database that will provide various data and meta-data for all of California's 20,000+ highway bridges. Beyond the immediate objectives of the present study, this database will have the potential to be useful to a broad array of experts from multiple domains—e.g., bridge engineers, city and traffic planners, and first responders—to carry out tasks such as emergency traffic planning, load rating of older bridges, life-cycle cost-benefit assessment of a given bridge.

The second objective is to devise a computational workflow that use the metadata from the database to produce a regional seismic risk/loss assessment of a given network of bridges. The said workflow produces quantitative results in the form of site- and structure-specific seismic bridge fragilities, which will enable pre-event regional damage and loss studies.

The third objective is to utilize the physical damage estimates for a given hypothetical/simulated seismic event to examine losses in regional traffic.

The fourth and final objective of this project is to demonstrate the utility of the aforementioned database and analysis workflow by applying it to the freight traffic to and from the Port of Los Angeles (POLB) and the adjacent Port of Long Beach (POLA) in the aftermath of a large Southern California scenario-based earthquake to examine resulting losses to regional traffic and the recovery times.

It is important to note that the aforementioned database and analysis tools will be expendable to a plethora of other applications related to the utility, functionality, and natural and anthropogenic hazard exposure of California's transportation network.

Organization of this document

Remainder of this document is organized as follows: First, the modeling procedures utilized to develop nonlinear time-history models of ordinary (single or multi-span) concrete bridges, which form the great

majority of California's bridge inventory, are provided. The construction of these models require metadata for each bridge. In the following section the descriptions of a series of algorithms that are based on image processing as well as various heuristics are provided, which collectively automate the extraction (or estimation) of geometry and other configurational metadata from street view and satellite images as well as standard design guideline documents. Next, a procedure is described that combines site- and structure-specific fragility functions for estimating damage to each bridge in a network, and a regional traffic model for estimating the losses to regional traffic flow, and the system's recovery.

Finally, a detailed the case study involving 1,000 bridges that surround the Ports of Los Angeles and Long Beach is carried out. This case study examines the consequences of a hypothetical large seismic event due to the rupture of the Palos Verdes fault, which is approximately 20 miles offshore from the two neighboring ports.

Methodology

Structural modeling of bridges

Content Regional seismic risk assessment requires an inventory of structural models. This chapter first describes the material and component models, as well as the mass and damping calculation procedures utilized to establish the bridge structural models. The ability of these modeling procedures to satisfactorily capture bridge response is dependent on the quality of the modeling properties used in defining the structural models. In determining appropriate modeling parameters, the author strongly benefited from the existing literature, specifically work done by Mangalathu and co-workers (*17*); hence these findings are briefly discussed. Particularly when modeling uncertainties are explicitly considered, defining the connection between seismic demands and structural damage is most easily established through fragility functions. Hence, lastly, the procedure utilized for calculating fragility curves at an individual bridge level is discussed.

The bridges considered consist of *reinforced concrete structures* with *prestressed concrete decks* supported by *seat*, *diaphragm*, or *cantilever* abutments. Most long-span bridges also incorporate *in-span hinges*. All of these details are explicitly considered in obtaining structural models from image-based geometric models.

The primary motivation behind this research is to develop a set of tools that can be easily applied to regional studies. For this purpose, a program that automatically generates structural models from the geometric information was devised. The program exclusively uses OpenSees (*18*). Although the details of OpenSees are not discussed here, when appropriate, reference is made to its commands specific to the performed implementation.

Material models

Concrete

In defining the stress-strain behavior of core and cover concrete, the concrete model proposed by Mander et al. (*19*) is used. The confined and unconfined concrete is defined in OpenSees using Popovics' concrete model with degraded linear unloading/reloading stiffness, Concrete04, and linear tension softening

concrete material, Concrete02 (*20*). Following Caltrans Seismic Design Criteria (*21*), for the unconfined (cover) concrete, the ultimate stress f_{co}', corresponding compressive strain ε_{co}', and the ultimate strain ε_{sp}' values are defined as equal to the expected compressive strength of unconfined concrete f_{ce}', 0.002, and 0.005, respectively, where

$$\boldsymbol{f_{ce}'} = \max(\mathbf{1.3}\boldsymbol{f_c}', \mathbf{5000}\text{psi}) \tag{1}$$

given f_c' denotes the specified compressive strength of unconfined concrete.

The ultimate stress of the confined concrete is determined using the relationship

$$\boldsymbol{f_{cc}'} = \boldsymbol{f_{co}'}\left(\mathbf{-1.254} + \mathbf{2.254}\sqrt{\mathbf{1} + \frac{\mathbf{7.94}\boldsymbol{f_{l'}}}{\boldsymbol{f_{co'}}}} - \mathbf{2}\frac{\boldsymbol{f_{l'}}}{\boldsymbol{f_{co'}}}\right) \tag{2}$$

The equation that defines the effective lateral confining pressure on concrete f_l' is determined by the shape of the cross section. For circular sections with hoop- or spiral-type transverse reinforcement,

$$f_l' = \frac{1}{2}k_e\rho_s f_{yh} \tag{3}$$

where ρ_s signifies the ratio of volume of transverse confining steel to volume of confined (core) concrete, f_{yh} denotes the yield strength of transverse reinforcement, and k_e is the confinement effectiveness coefficient. ρ_s is defined in terms of transverse reinforcement area A_{sp}, transverse reinforcement diameter d_b, and center-to-center spacing (pitch) of transverse reinforcement s as $\rho_s = 4A_{sp}/d_s s$. The confinement effectiveness for circular sections confined by circular hoops is determined as

$$k_e = \frac{\left(1-\frac{s'}{2d_s}\right)^2}{1-\rho_{cc}} \tag{4}$$

Similarly, the confinement effectiveness for sections confined by circular spirals is defined as

$$k_e = \frac{1-\frac{s'}{2d_s}}{1-\rho_{cc}} \tag{5}$$

where s', d_s, and ρ_{cc} denote clear spacing between hoops (or spiral), diameter of hoops (or spiral), and ratio of total longitudinal steel area to area of concrete core, respectively. Figure 1 outlines the geometric parameters required for specifying the behavior of confined core in circular sections.

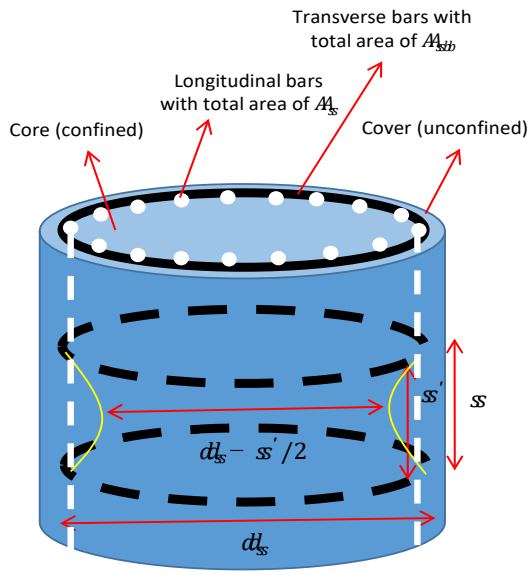

Figure 1. Geometric parameters used in defining confined behavior for circular sections.

For rectangular sections, due to potential differences in geometric configuration along the length (x-direction) and width (y-direction) of the section, a distinction is made in calculating for calculating $f_l{}'$ in x- and y-directions as

$$\boldsymbol{f_{lx}{}' = k_e \rho_x f_{yh}} \tag{6}$$

$$\boldsymbol{f_{ly}{}' = k_e \rho_y f_{yh}} \tag{7}$$

where ρ represents the total area of transverse bars running in the x- and y-directions, calculated as in terms of total areas of transverse reinforcement parallel to x- and y-axis A_{sx}, A_{sy}; center-to-center spacing of transverse reinforcement s; concrete core dimensions to center line of perimeter hoop in x- and y-directions b_c, d_c as

$$\boldsymbol{\rho_x = \frac{A_{sx}}{s d_c}} \tag{8}$$

$$\boldsymbol{\rho_x = \frac{A_{sy}}{s b_c}} \tag{9}$$

Note that $b_c \geq d_c$. The confinement effectiveness for rectangular sections is calculated using the relationship

$$\boldsymbol{k_e = \frac{\left(1 - \sum_{i=1}^{n} \frac{w_i{}'^2}{6 b_c d_c}\right)\left(1 - \frac{s'}{2 b_c}\right)\left(1 - \frac{s'}{2 d_c}\right)}{1 - \rho_{cc}}} \tag{10}$$

where w_i is the ith clear transverse spacing between adjacent longitudinal bars, s' is the clear spacing between hoop bars and n is the number of transverse bars. Figure 2 displays the geometric parameters defined in determining the confined concrete core behavior in rectangular sections.

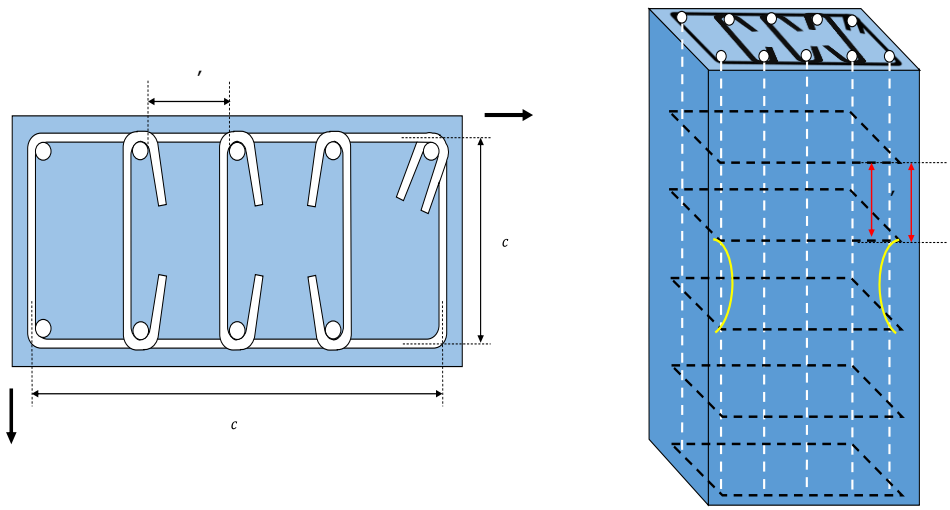

Figure 2. Geometry parameters used in defining confined behavior for rectangular sections.

The compressive strain at f_{cc}' is calculated using the relationship

$$\boldsymbol{\varepsilon_{cc} = \varepsilon_{co}\left[1 + 5\left(\frac{f_{cc'}}{f_{co'}} - 1\right)\right]} \tag{11}$$

The compressive strain value where strain energy equilibrium between the concrete and the confinement steel is reached, i.e., ε_{cu}, is defined as 0.025.

Lastly, the modulus of elasticity for concrete is defined using the relationship

$$\boldsymbol{E_c = 33w^{1.5}\sqrt{f_{ce}'}} \tag{12}$$

where w denotes the unit weight of concrete in lb/ft^3, and E_c and f_{ce}' are as previously defined, in units of psi. Furthermore, the shear modulus of concrete is calculated as

$$\boldsymbol{G_c = \frac{E_c}{2(1+v_c)}} \tag{13}$$

where $v_c = 0.2$. Figure 3 provides a summary of the characteristics specified for simulating concrete behavior.

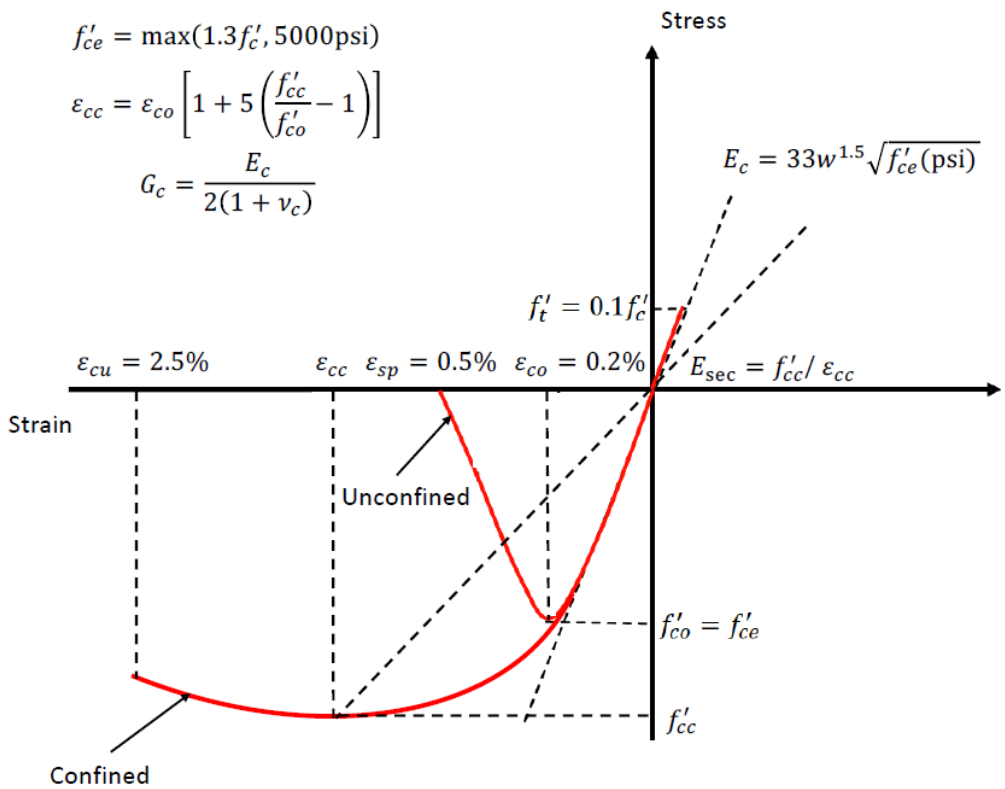

Figure 3. Stress-strain backbone curves for concrete.

Steel

ASTM A706 Grade 60 steel reinforcement is used in modeling the reinforcement. The stress-strain behavior of Grade 60 steel is displayed in Figure 4. In OpenSees, this material is implemented using the Chang and Mander (*22*) uniaxial steel model, i.e., the ReinforcingSteel object.

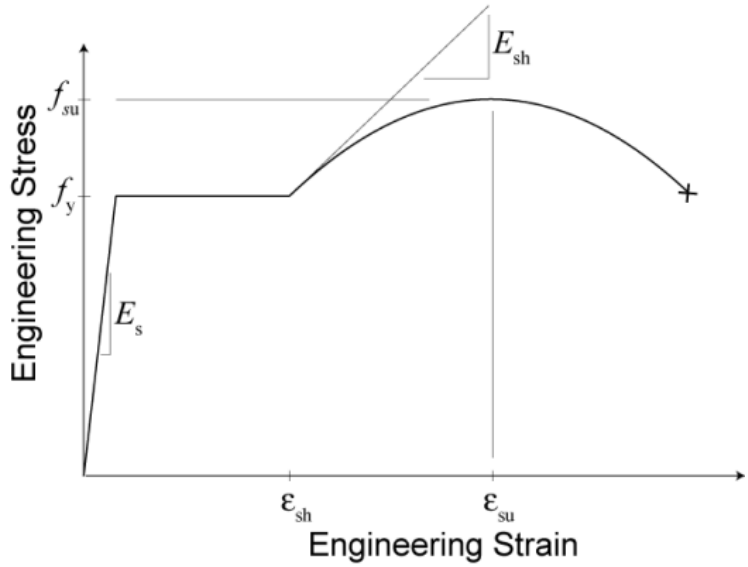

Figure 4. Stress-strain curve for the reinforcement steel.

Table 1 shows the material properties for ASTM A706 Grade 60 steel. Other than the expected tensile strength f_{ue}, all material traits of the reinforcing steel are defined according to Caltrans SDC requirements. f_{ue} is randomly sampled from existing class statistics for California bridges as described in Model Properties.

Table 1. Material properties of the reinforcing steel adopted in bridge models

Property	Value
Modulus of Elasticity, E_s	29,000 ksi
Expected yield strength, f_{ye}	discussed in text
Expected tensile strength, f_{ue}	95 ksi
Expected yield strain, ε_{ye}	0.0023
Ultimate tensile strain, ε_{su}	0.120 for #10 bars and smaller 0.090 for #11 bars and larger
Reduced ultimate tensile strain, ε_{su}^{R}	0.090 for #10 bars and smaller 0.060 for #11 bars and larger
Strain at onset of strain hardening, ε_{sh}	0.0150 for #8 bars 0.0125 for #9 bars 0.0115 for #10 & #11 bars 0.0075 for #14 bars 0.0050 for #18 bars

Component models

Columns

Columns are critical to the load-carrying capacity of bridge structures after an earthquake. Hence, carefully quantifying their performance is essential for accurate simulations of bridge behavior under earthquake excitations. Column seismic response is an aggregate of axial-flexural, shear, and torsional behavior; thus, considering each of these effects in detail is vital to estimate post-earthquake damage susceptibility of columns.

The axial-flexural behavior of columns is largely inelastic, where the levels of transverse reinforcement determine the extent of inelasticity. In this study, the inelastic column behavior due to flexural loading, spreading of plasticity across the column cross-section and length are computed using fiber sections where moment-curvature and axial force-deformation characteristics and their interaction are explicitly considered. For this purpose, each column is modeled using a beam-column element based on force-based formulation. As discussed by Neuenhofer and Filippou (*23*), force-based elements utilize exact force interpolation functions, hence their solution is only susceptible to a numerical integration error. This error is minimized for a column by increasing the number of elements, or integration points used to define that column. Consequently, given reducing the number of elements results in a more computationally efficient implementation, here, each column is represented with a single element with ten integration points. In OpenSees fiber section definitions are performed using the fiberSec object and patch commands. The cover concrete and core concrete are assigned unconfined and confined concrete properties (defined in the previous) as shown in Figure 5. The force-based beam-column elements are implemented in OpenSees via forceBeamColumn object with Gauss-Radau (*24*) plastic hinge integration method.

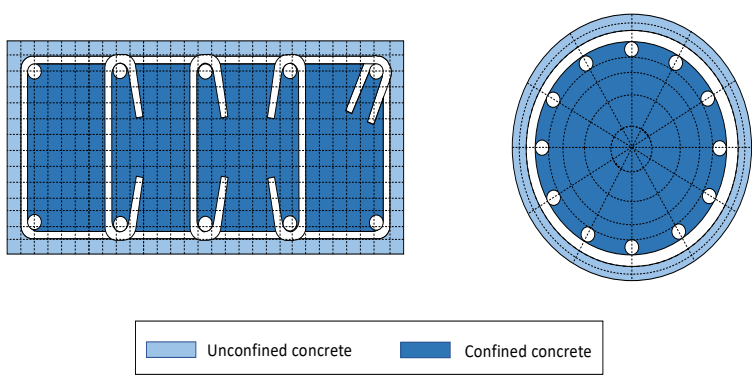

Figure 5. Fiber discretization of rectangular (left) and circular (right) reinforced concrete column sections

The column shear deformations are considered in the analyses using an elastic material with shear stiffness of kG_cA_c, where A_c is the cross-sectional area of the column, and k denotes the shear correction factor determined based on the cross-sectional shape. The torsional column deformations are also incorporated using an elastic material. The torsional stiffness of the material is calculated using the relationship $0.2GcJc$, suggested by Aviram et al. (*25*), where Jc is the second moment of area of the column section, and 0.2 is the stiffness reduction factor that considers section cracking. Lastly, to compute the combined column force-deformation behavior, the individual force-deformation responses of the defined fiber, shear, and torsional materials are aggregated. In OpenSees this aggregation is performed using the Aggregator construct.

The parts of columns embedded in the superstructure are modeled by defining a weightless rigid element from the top of the nonlinear beam-column element to the geometric centroid level of the superstructure. In the case of multi-column bridges, the rigid elements between the top node of columns to the centroid level of the superstructure are also connected using weightless rigid links. This horizontal connection between columns is fully restrained to the superstructure using diaphragm constraint and facilitates the transfer of force and moment between the column elements. Figure 6 shows typical beam-column/rigid link assemblies for single column and multi-column bridges.

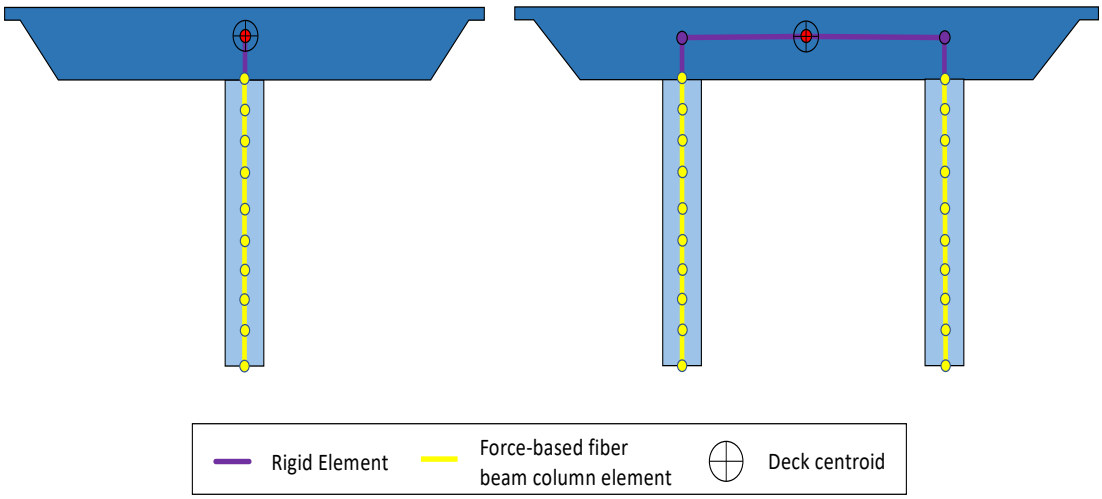

Figure 6. Beam-column/rigid link assemblies used in modeling single-column (left) and multi-column (right) bridge bents.

Column foundations are modeled using linear translational and rotational springs—with stiffnesses K_t and K_r, respectively—aligned with the directions longitudinal and transverse to the bridge deck. Figure 7 shows the geometric representation of a foundation spring assembly for a bridge segment containing a single-column bridge bent. In OpenSees, foundation springs are generated using a zeroLength element containing all four springs in the foundation assembly.

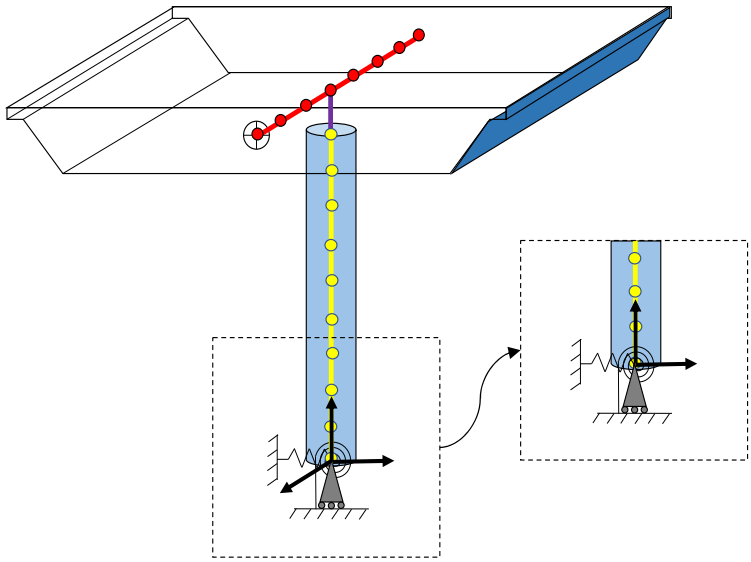

Figure 7. Spring idealization of soil-foundation interaction at the base of bridge columns.

Superstructure

According to AASHTO specifications (*26*), superstructures of non-seismically isolated reinforced concrete bridges are designed as capacity protected members. Hence, their seismic response is essentially elastic. Consequently, for computational efficiency, reinforced concrete decks can be idealized as a linear assembly of elastic beam-columns elements running through the geometric centroid of the deck, as previously shown in Figure 7. In modeling regular reinforced concrete deck sections, to correctly determine the vibration periods and the seismic demands, cracked (effective) section moment of inertia I_{eff} of $0.75I_g$ is utilized (*27*). For prestressed superstructure constructions, stiffness reduction is not performed, as per Caltrans (*21*) recommendations.

In-span Hinges

In long and continuous RC box-girder bridges, potential stresses due to temperature variations, creep, and shrinkage are reduced by the use of in-span hinges. In-span hinges effectively divide a structure into shorter frames by permitting relative displacements between adjacent deck segments in longitudinal and transverse directions. In an in-span hinge, the vertical forces between adjacent deck segments are transferred by supporting the long cantilever segment of the span on the short cantilever through a number of bearings. Under operational conditions, in-span hinges are expected to develop a minimal amount of stress in transverse and longitudinal directions. However, during severe earthquakes, out-of-phase vibrations may be induced in adjoining frames; consequently, large relative displacements may occur. Internal shear keys and elastomeric bearings provided in in-span hinges limit these large displacements in the transverse direction. In the longitudinal direction, relative movement is restrained by the lateral resistance of the bearings and shear keys, as well as the resistance of the hinge back wall. Figure 8 shows the side view of a typical in-span hinge connection. From a modeling perspective, the interactions between adjacent frame segments due to in-span hinge behavior can be simulated by coupling the end nodes of each deck segment to the respective nodes of a zero-length element

(zeroLength in OpenSees) assembly, as shown in Figure 8. Figure 9 provides a schematic view of the principal load-resisting components of an in-span hinge.

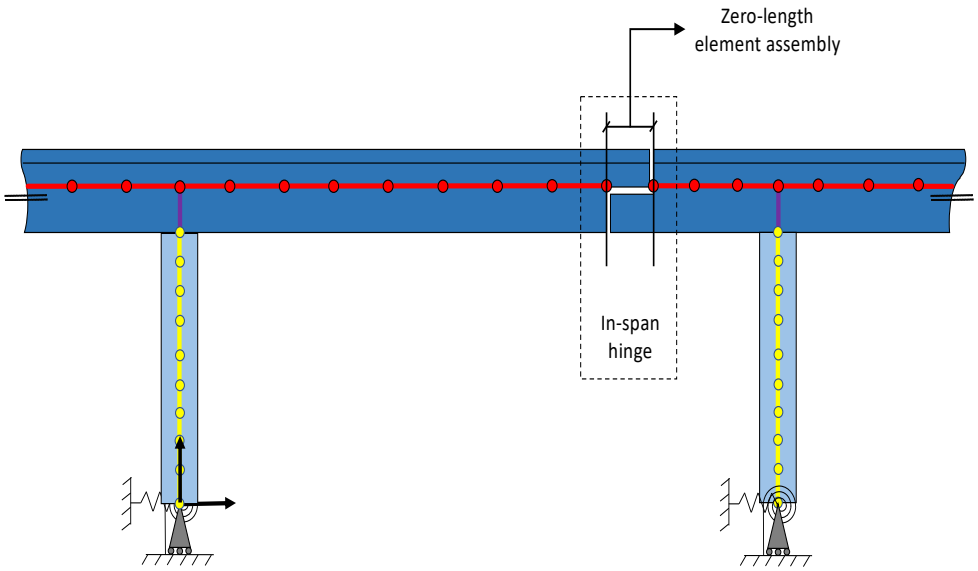

Figure 8. Elevation view of a bridge in-span hinge.

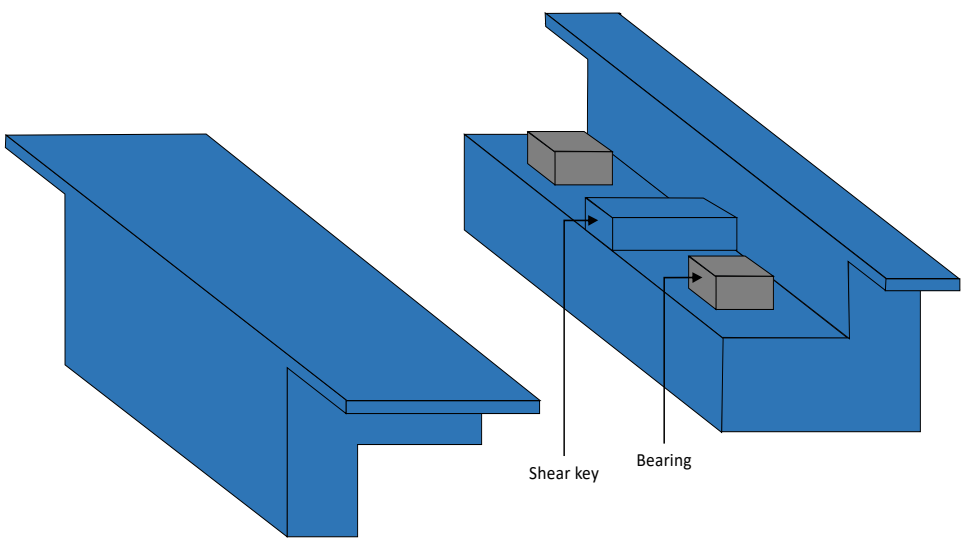

Figure 9. Schematic view of a typical in-span hinge.

Longitudinal behavior of in-span hinges

Three components determine the longitudinal behavior of in-span hinges, namely elastomeric bearings, internal shear keys, and the hinge back wall. Lateral resistance of the bearing pads is assumed to follow the elastic-perfectly plastic behavior shown in Figure 10. The shear capacity of the bearings is controlled by the friction coefficient μ between the pads and the bearing seat, and the vertical force supported by each bearing N_b. For a single bearing, the yielding deformation is determined by dividing the yielding force V_{yb} for the bearing by its elastic stiffness k_b. According to Caltrans (*21*), the maximum shear strain a

bearing can sustain before failure Δ_{mb} is 1.5 in both tension and compression. In OpenSees, the force-deformation behavior of elastomeric pads is defined using the uniaxial bilinear material object Steel01.

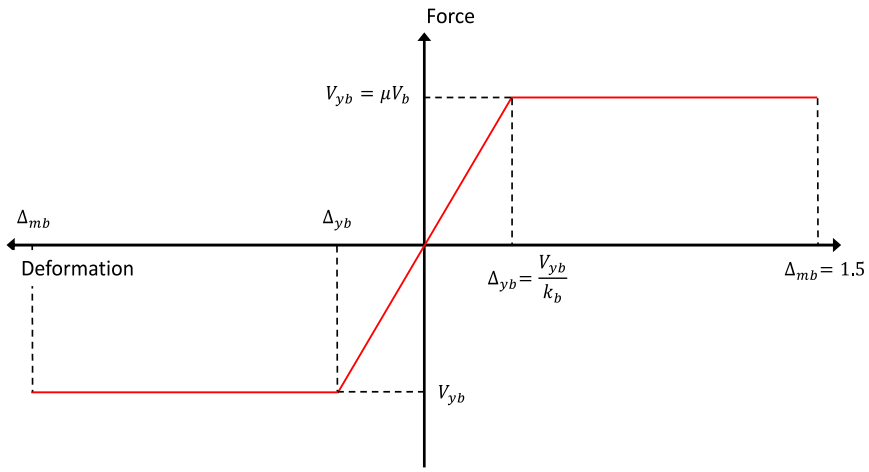

Figure 10. Lateral force-deformation behavior of elastomeric bearings.

The behavior of shear keys is defined through a strain-softening gap material that follows the force-deformation relationship shown in Figure 11, as suggested by Mangalathu (*17*). The shear key capacity is determined as the product of the superstructure dead load at the in-span hinge seat P_{dl} and the acceleration levels the shear key is designed to withstand β. The shear key lateral resistance is assumed to reach zero subsequent to plastic deformation of 3.5 inches. Note that plastic deformation is calculated as the difference between maximum permitted deformation Δ_{mk}, and the gap between the superstructure and shear key Δ_{gk}. In OpenSees, the force-deformation relationship for in-span hinge shear keys is defined using the elastic-perfectly plastic gap uniaxial material object ElasticPPGap.

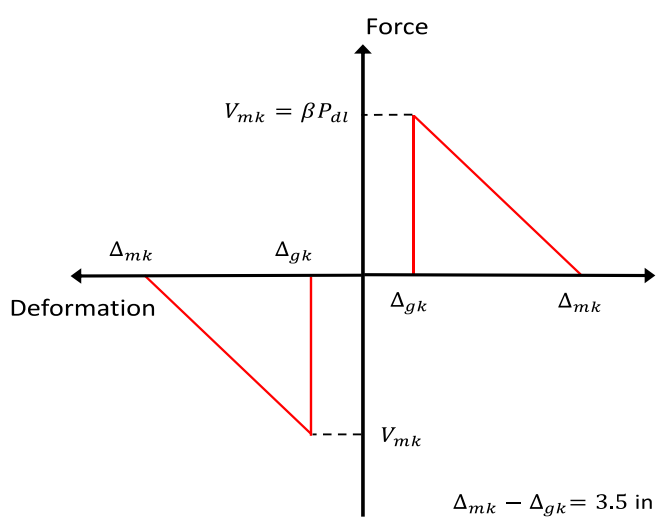

Figure 11. Force-deformation relationship for in-span hinge shear key elements.

Longitudinal resistance of the seat back wall is modeled using the simplified impact model proposed by Muthukumar (*28*). Force-deformation response of the back wall is characterized by the parameters: initial gap Δ_{gbw}, yield deformation Δ_{ybw}, maximum deformation Δ_{mbw}, initial stiffness k_{1bw}, and strain

hardening stiffness k_{2bw}, as shown in Figure 12. For the bridge models developed for this study, Δ_{ybw}, Δ_{mbw}, k_{1bw}, and k_{2bw} are assumed 0.1 in, 1 in, 1022.3 kip/ft, and 351.76 kip/ft, respectively. Back wall response is defined in OpenSees via the ImpactMaterial object.

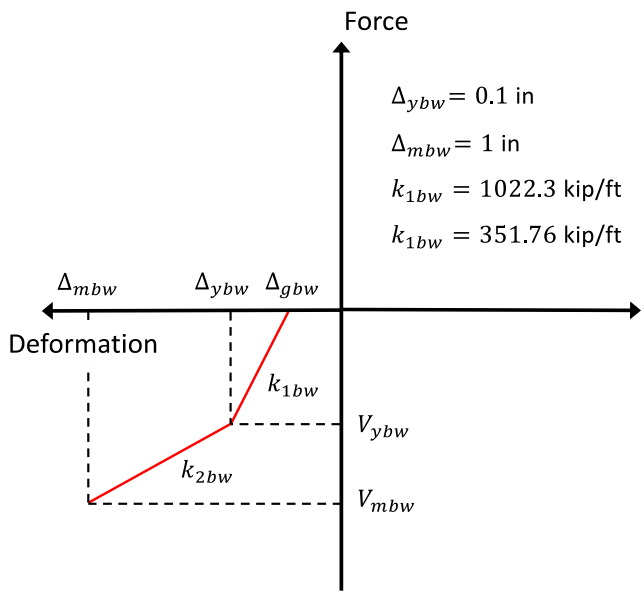

Figure 12. Force-deformation response of an in-span hinge back wall.

Transverse behavior of in-span hinges

In-span hinge behavior in the transverse direction is controlled by the lateral resistance shear key and elastomeric bearing elements. The force-deformation behaviors of these elements are identical in longitudinal and transverse directions; hence they are not restated.

Vertical behavior of in-span hinges

The vertical resistance of an in-span hinge is defined by the seat total shear resistance, calculated by combining the contributions of reinforcing steel and concrete. Figure 13 shows the geometric parameters significant to the seat behavior.

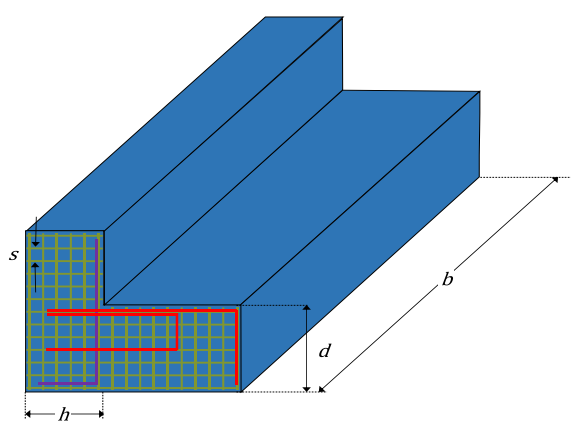

Figure 13. Typical in-span hinge seat reinforcement detailing.

The force-deformation relationship for the reinforcing steel is determined by the reinforcement shear capacity V_{ss} and the initial deformation at which the shear capacity is reached Δ_{1s}, as shown in Figure 14. According to Hube and Mosalam (*29*),

$$\boldsymbol{V_{ss} = A_{s1} f_{ye} + A_{s2} f_{ye}} \tag{14}$$

where A_{s1} and A_{s2} are the total steel areas for the tension tie (denoted as purple in Figure 13) and the first row of reinforcement crossing the back wall/seat interface (denoted as red in Figure 13), respectively. Megally et al. (*30*) recommend the use of the following expression to calculate the deformation value Δ_{1s}.

$$\boldsymbol{\Delta_{1s} = \sqrt{2}\epsilon_{ye}(L_d + L_a)\frac{h+d}{\sqrt{h^2+d^2}}} \tag{15}$$

where, as defined in Figure 13, h and d denote seat height and back wall length, respectively. Experimental results indicate that the extent of the crack region is approximately equal to the seat width (*30*), i.e., $L_a = b$. On the other hand, the reinforcement development length L_d is given by Priestley at al. (*31*) as

$$\boldsymbol{L_d = \frac{d_b f_{ye}}{25\sqrt{f_{ce}'}}} \tag{16}$$

where d_b is the nominal bar diameter in inches. In the equation above, both f_{ye} and f_{ce}' are defined in psi.

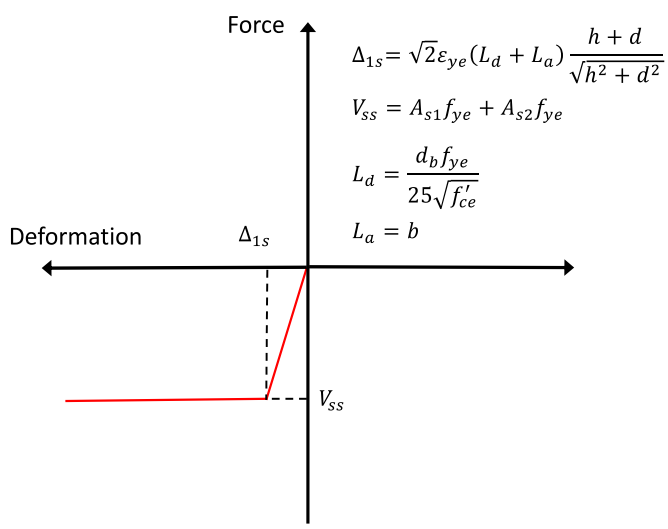

Figure 14. Force-deformation relationship for the contribution of steel reinforcement to the vertical resistance of an in-span hinge seat.

The force-deformation relationship for the concrete is defined in terms of three parameters: concrete shear strength V_{cs}, the corresponding concrete deformation Δ_{2s}, and the deformation at which the shear capacity of concrete is reduced to zero Δ_{3s}, as shown in Figure 15. Concrete shear contribution V_{cs} is calculated as

$$\boldsymbol{V_{cs} = 2.4\sqrt{f_{ce}'}bd} \tag{17}$$

where $f_{ce}{}'$ is defined in psi, and b and d denote the seat width and back wall length, respectively (see Figure 13). As reported by Megally et al. (*32*), Δ_{2s} is given by

$$\boldsymbol{\Delta_{2s} = \sqrt{2}\epsilon_{ye}(L_d + L_a)\frac{h+d}{s}} \tag{18}$$

Lastly, according to Silva et al. (*31*), Δ_{3s} is determined through the relationship

$$\boldsymbol{\Delta_{3s} = \sqrt{2}\epsilon_{3}(L_d + L_a)\frac{h+d}{s}} \tag{19}$$

In equations above, s is the spacing for the reinforcement within the seat, $\epsilon_3 = 0.005$. The remaining parameters are as defined before.

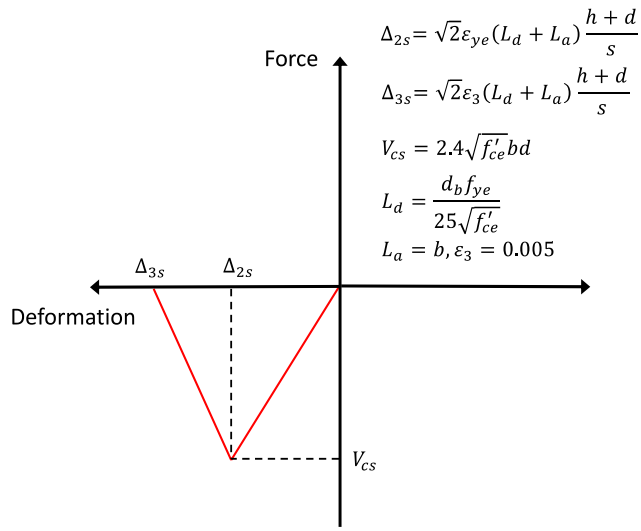

Figure 15. Force-deformation relationship for the contribution of concrete to the vertical resistance of an in-span hinge.

By combining the contributions of the steel reinforcement and concrete in parallel, the force-deformation curve shown in Figure 16 is obtained for the vertical resistance of the in-span hinge seat. In OpenSees, the contribution to the vertical seat resistance by the reinforcing steel, shown in Figure 14, is defined using the uniaxial Bilin material object. The concrete contribution displayed in Figure 15 is defined using the uniaxial zero tensile strength concrete material object Concrete01. The force-deformation relationships for the steel reinforcement and concrete are combined in parallel using the Parallel uniaxial material object in OpenSees.

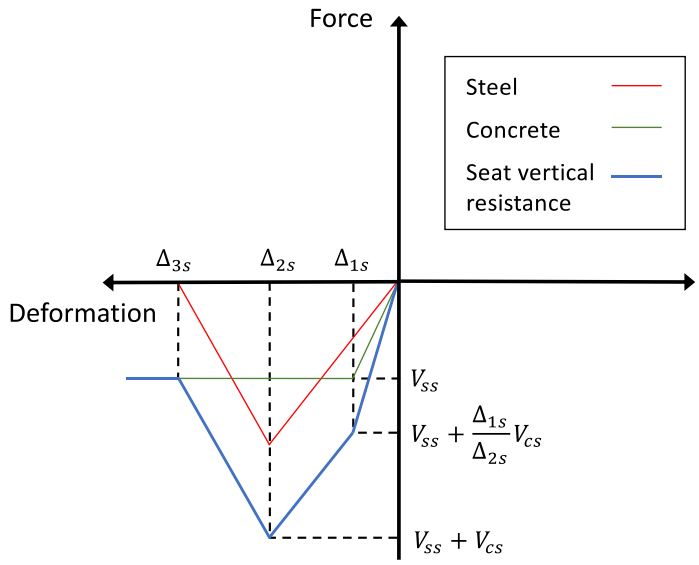

Figure 16. Force-deformation relationship for the vertical resistance of an in-span hinge.

Macroelement assembly for in-span Hinges

Figure 17 shows the final zero-length element assembly used to define nonlinear in-span hinge behavior. Note that weightless rigid elements (denoted as purple in Figure 17) are attached to the end nodes of each deck segment to consider the rotational response appropriately. Force-deformation characteristics of the in-span hinge back wall and seat are calculated as in Figure 12 and Figure 16, and the determined resistances are equally divided among the respective spring elements. In order to define the elastomeric bearing and shear key resistances in the transverse direction, the total contribution of each component is calculated via scaling the relationships in Figure 10 and Figure 11 by the number of components, then the obtained resistances evenly distributed among the respective springs.

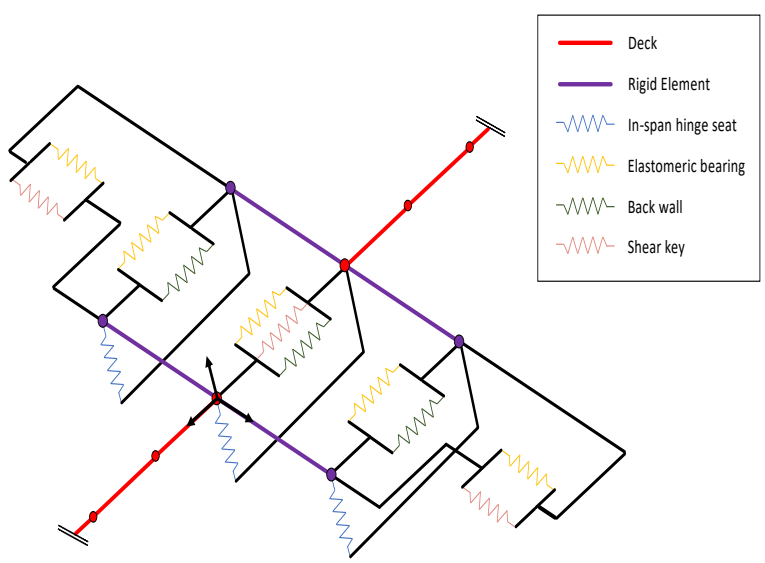

Figure 17. Zero-length element assembly for an in-span hinge connection.

Abutments

At each end of a bridge, the superstructure is supported by abutments. The primary purpose of abutments is to transfer the vertical and horizontal loads from the superstructure to the abutment foundations and retain the lateral loads from roadway embankment under both operational and extreme loading conditions. In terms of the rigidity of the connection to the superstructure, abutments are classified as integral and non-integral. Diaphragm and seat-type abutments are the most common examples of integral and non-integral abutments, respectively. Figure 18 and Figure 19 show the side views of these two abutment types. Figure 20 shows the components of a typical seat-type abutment.

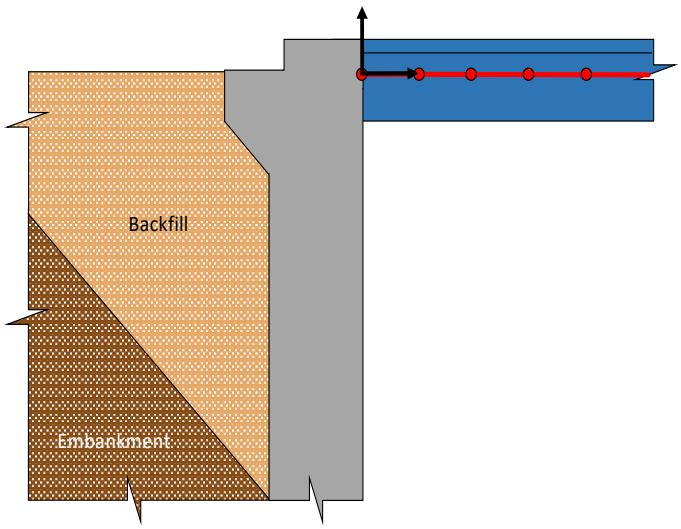

Figure 18. Diaphragm abutment.

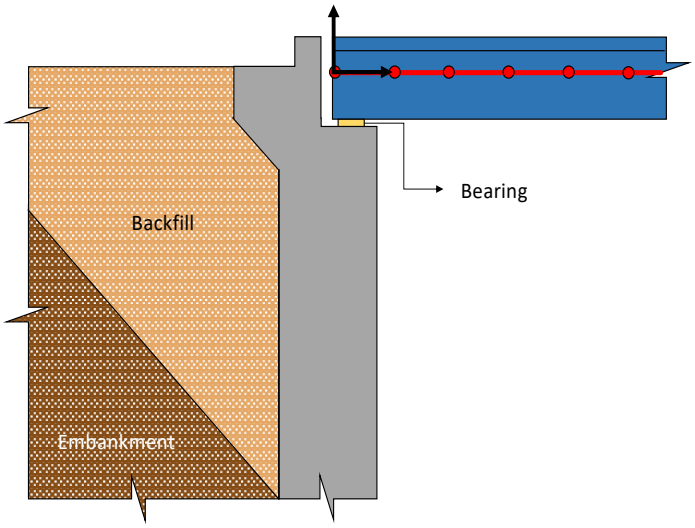

Figure 19. Seat-type abutment.

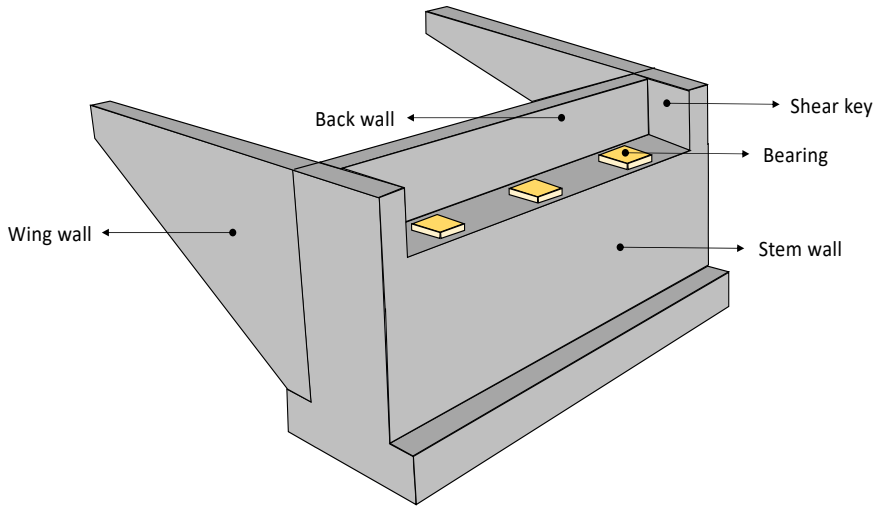

Figure 20. Components of a seat-type abutment.

The diaphragm abutment is built monolithic to the bridge superstructure. The abutment is connected straight to abutment foundations, and its diaphragm is in direct contact with the embankment. As a result of this simpler construction, diaphragm abutment induces lower initial construction costs. Its application, however, is limited to short-length bridges, since it is less amenable to large superstructure movements due to temperature variations, creep and shrinkage, and post-tensioning compared to non-integral abutment types.

The seat-type abutment is not integral to the superstructure and acts as an independent structural component of the bridge. In a seat abutment, the superstructure is supported by the bearings on the abutment seat. The lateral soil pressure is mostly resisted by the stem wall, with just the portion of the backfill above the seat level retained by the back wall. Superstructure movements in longitudinal and transverse directions are restrained by the back wall and the shear keys, respectively. Unlike in diaphragm abutments, the gap between the superstructure and back wall/shear keys provides added stress relief for temperature, creep and shrinkage, or post-tensioning induced deformations. That renders seat-type abutments more suitable to long, highly skewed, or curved bridges than diaphragm abutments. Unseating of the superstructure is a critical mode of failure for seat-type abutments, resulting in the collapse of the end span. Thus, to eliminate unseating, modern-day seat-type abutments are designed with large seat widths.

Abutment behavior in the longitudinal direction

The longitudinal behavior of a diaphragm abutment is characterized by the lateral resistance of abutment piles and the passive resistance of the abutment backfill. Following the approach presented by Mangalathu (*17*), lateral resistance of abutment piles is modeled using the trilinear force-deformation relationship displayed in Figure 21. The initial yield deformation Δ_{1p} and plastic yield deformation Δ_{2p} are set to 6 mm and 25 mm, respectively. The yield force V_{1p} is set equal to half the plastic yielding force V_{2p}. In OpenSees, the force-deformation behavior of abutment piles is captured using the uniaxial bilinear hysteretic material object Hysteretic with pinching factors during reloading for strain and stress set to 0.75 and 0.5, respectively, according to Ramanathan et al. (*32*).

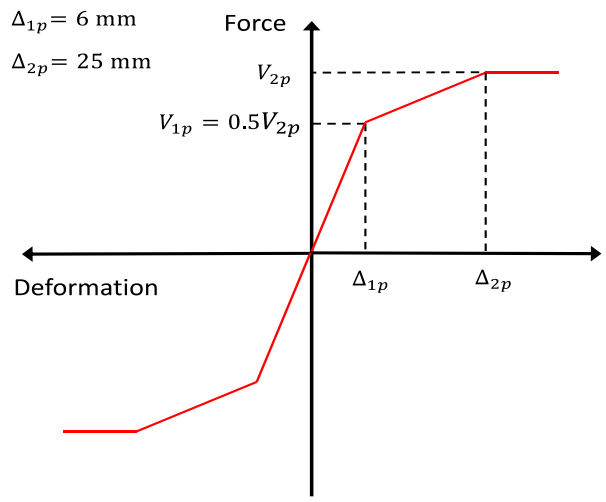

Figure 21. Force-deformation relationship for abutment piles.

Passive longitudinal resistance of abutment backfill is defined using the Generalized Hyperbolic Force–Displacement (GHFD) backbone curve proposed by Khalili-Tehrani et al. (*33*). Figure 22 shows the force-deformation response of homogeneous backfill material as defined by GHFD. The change in lateral resistance of the backfill material $V_{bw}(\Delta)$ is defined in terms of lateral displacement Δ as

$$\boldsymbol{V_{bw} = f_{\delta} \frac{a_r \Delta}{\hat{H} + b_r \Delta} \hat{H}^{n_{bw}}} \tag{20}$$

for

$$\boldsymbol{\hat{H} = \frac{H_{bw}}{H_r}} \tag{21}$$

$$\boldsymbol{a_r = \frac{1}{\beta_{bw}}(\eta - 1)\alpha} \tag{22}$$

$$\boldsymbol{b_r = \frac{1}{\beta_{bw}}(\eta - 2)} \tag{23}$$

where H_{bw} is the backwall height, H_r is the reference back wall height of 3.2808 ft, the wall friction adjustment factor $f_\delta = 1$, and

$$\boldsymbol{\beta_{bw} = [670.47 - 269.05(\tan\phi)^{1.23}]\varepsilon_{50}} \tag{24}$$

$$\boldsymbol{\alpha = [60.49(\tan\phi)^2 + 5.74]\gamma + [34.71(\tan\phi)^{1.79} + 9.37]c} \tag{25}$$

$$\boldsymbol{n_{bw} = \frac{0.13(\tan\phi)^{1.2} + 0.22}{\sqrt{c}} + 0.9} \tag{26}$$

$$\boldsymbol{\eta = 18.10 - 9.38\sqrt{tan\phi}} \tag{27}$$

Recognizing that silty sand is the most common abutment backfill material (*34*), in the generated bridge models, unit weight γ, internal friction angle ϕ, cohesion c, and strain at 50% ultimate strength ε_{50} are respectively set to 0.125 kcf, 40°, 0.3 ksf, and 0.5% after Stewart et al. (*35*).

In OpenSees, the backfill material is defined using the HyperbolicGapMaterial object with zero gap. The initial stiffness k_{max} and unloading/reloading stiffness k_{ur} of the hyperbolic material is determined using the relationship

$$\boldsymbol{k}_{\text{max}} = \boldsymbol{k}_{\text{ur}} = \boldsymbol{f}_{\boldsymbol{\delta}}\boldsymbol{a}_{\boldsymbol{r}}\widehat{\boldsymbol{H}}^{\boldsymbol{n}_{\boldsymbol{bw}}-\mathbf{1}} \tag{28}$$

The ultimate strength $V_{\text{ult}_{bw}}$ of the material is calculated by setting Δ equal to the maximum deformation Δ_{mbw}. According to Shamsabadi et al. Δ_{mbw} for silty sand backfill materials is determined as

$$\boldsymbol{\Delta}_{\boldsymbol{mbw}} = \mathbf{0.05}\boldsymbol{H} \tag{29}$$

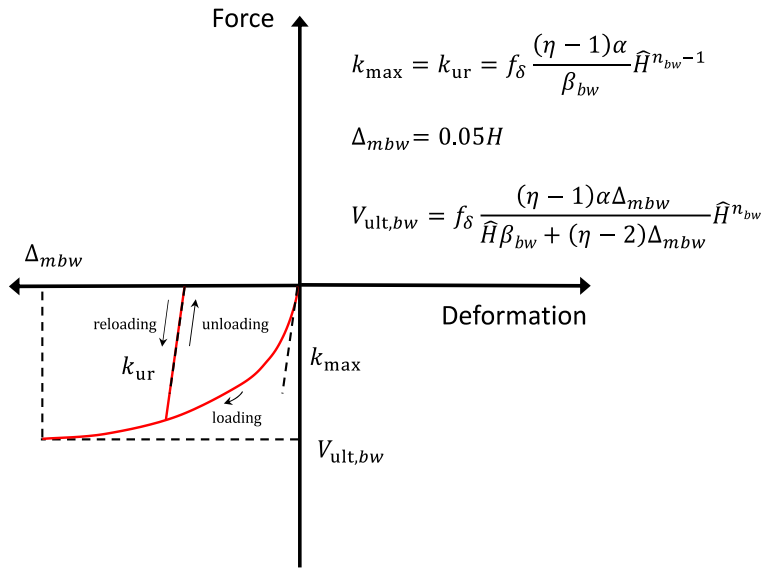

Figure 22. Force-deformation relationship for abutment backfill.

In seat-type abutments, lateral resistances of the abutment back wall and elastomeric bearings are also critical in resembling the longitudinal abutment behavior. Contributions of back wall and bearings are defined according to the force-displacement relationships described earlier.

Abutment behavior in the transverse direction

The transverse behavior of a diaphragm abutment is determined by the lateral resistance of abutment piles alone. Lateral abutment pile response is assumed identical in both the longitudinal and transverse directions, hence it is modeled according to the force-deformation curve defined earlier.

In a seat-type abutment, however, elastomeric bearings and shear keys also contribute to the abutment resistance in the transverse direction. Bearings follow the elastic-perfectly plastic force-deformation behavior described earlier. The transverse resistance of each shear key is defined as the combined shear resistance from the shear key reinforcing steel and concrete. The geometric parameters critical to shear key behavior are displayed in Figure 23.

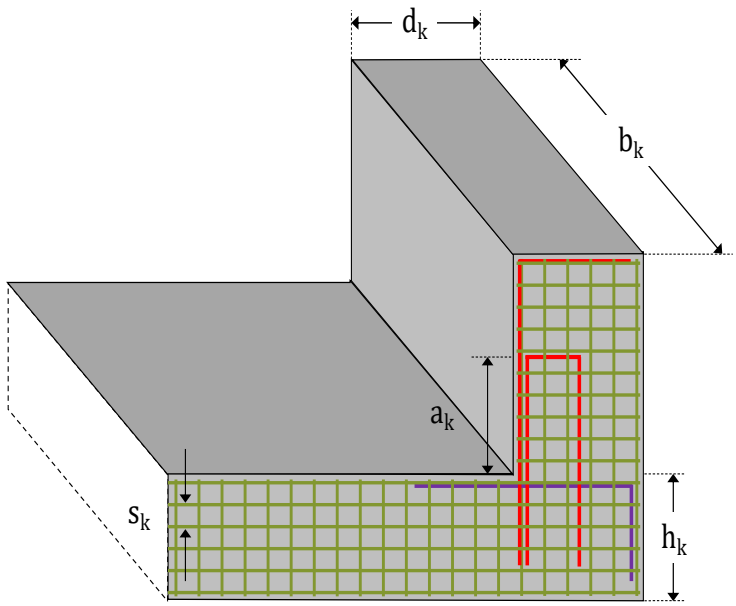

Figure 23. Typical abutment shear key reinforcement detailing.

According to Silva et al. , the force-deformation relationship for the reinforcing steel is defined in terms of reinforcement shear capacity V_{sk}, initial deformation at which the shear capacity is reached Δ_{1k}, deformation corresponding to initial softening Δ_{4k}, and ultimate shear deformation Δ_{5k} as shown in Figure 24. The reinforcement shear capacity is calculated as

$$\boldsymbol{V_{sk}} = \frac{\boldsymbol{f_{ye}}}{\boldsymbol{h_k + a_k}}\left[(\boldsymbol{A_{k1}} + \boldsymbol{A_{k2}})\boldsymbol{h_k} + \frac{\boldsymbol{A_{ks}}}{\boldsymbol{2s_k}}\left(\boldsymbol{n_v h_k^2} + \boldsymbol{n_h d_k^2}\right)\right] \tag{30}$$

where A_{k1}, A_{k2}, A_{ks} are the total steel areas for the tension tie (denoted as purple in Figure 23), the first row of reinforcement crossing the abutment seat/shear key interface (denoted as red in Figure 23), and the side reinforcement (denoted as green in Figure 23), respectively. n_h and n_v signify the numbers of side faces with horizontal and vertical side reinforcement, respectively. h_k, a_k, and s_k are as defined in Figure 23.

The following equations are utilized to calculate Δ_{1k}, Δ_{4k}, and Δ_{5k}.

$$\begin{aligned} \boldsymbol{\Delta_{1k}} &= \sqrt{\boldsymbol{2}}\boldsymbol{\epsilon_{ye}}(\boldsymbol{L_d} + \boldsymbol{L_a})\frac{\boldsymbol{h_k + d_k}}{\sqrt{\boldsymbol{h_k^2 + d_k^2}}} \\ \boldsymbol{\Delta_{4k}} &= \sqrt{\boldsymbol{2}}\boldsymbol{\epsilon_4}(\boldsymbol{L_d} + \boldsymbol{L_a})\frac{\boldsymbol{h_k + d_k}}{\boldsymbol{s_k}} \\ \boldsymbol{\Delta_{5k}} &= \sqrt{\boldsymbol{2}}\boldsymbol{\epsilon_5}(\boldsymbol{L_d} + \boldsymbol{L_a})\frac{\boldsymbol{h_k + d_k}}{\boldsymbol{s_k}} \end{aligned} \tag{31}$$

where, $L_a = b$, L_d is as defined previously, $\epsilon_4 = 0.007$, and $\epsilon_5 = 0.01$.

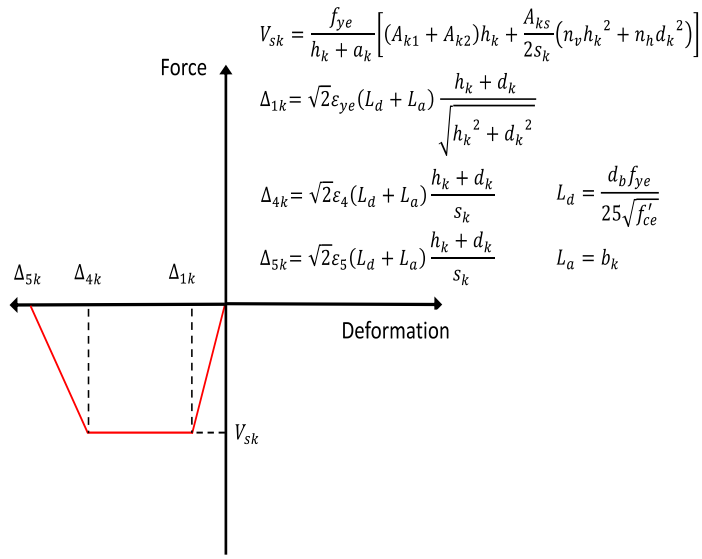

Figure 24. Force-deformation relationship for the contribution of steel reinforcement to the lateral resistance of an abutment shear key.

The contribution of concrete to abutment shear key capacity is determined as defined previously. The force-deformation relationship for the concrete contribution is as shown in Figure 15. Peak concrete contribution V_{ck}, Δ_{2k}, and Δ_{3k} are calculated using equations given earlier.

Combining the contributions of the steel reinforcement and concrete in parallel, and connecting this material in series to an elastic no-tension material to account for the gap between the deck and shear keys, the force-deformation curve shown in Figure 25 is obtained for the lateral resistance of an abutment shear key. In OpenSees, the contribution of reinforcing steel, shown in Figure 24, is prescribed using the uniaxial Bilin material object. The force-deformation curve for concrete displayed in Figure 15 is implemented using the uniaxial zero tensile strength concrete material object Concrete01. Compression-only gap element was defined using the elastic-perfectly plastic gap uniaxial material object ElasticPPGap where tangent stiffness is set to a very high value. The force-deformation relationships for the steel reinforcement and concrete are combined in parallel using the Parallel uniaxial material object. The combined concrete-steel material is connected in series with the gap element using the Series uniaxial material object in OpenSees.

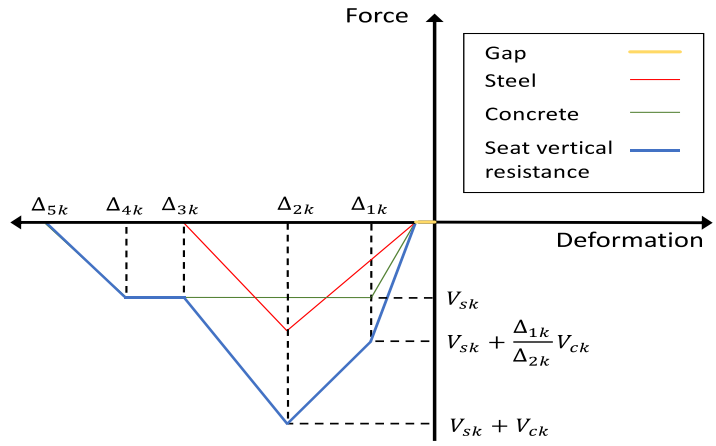

Figure 25. Force-deformation relationship for an abutment shear key.

Macroelement assembly for abutment behavior

Figure 26 shows the final zero-length element assembly used to define nonlinear abutment behavior for diaphragm and seat-type abutments. Force-deformation characteristics of the abutment piles are calculated as in Figure 21 and multiplied by the deck width to determine the longitudinal and transverse resistances of pile spring elements. Longitudinal resistance of the backfill springs is calculated by multiplying the force-deformation relationship in Figure 22 by the width of the backwall. As in the case of in-span hinges, to define the elastomeric bearing and shear key spring resistances in the transverse direction, the total contribution of each component is calculated via scaling the relationships in Figure 10 and Figure 25 by the number of components, then the calculated resistances are split among the respective springs.

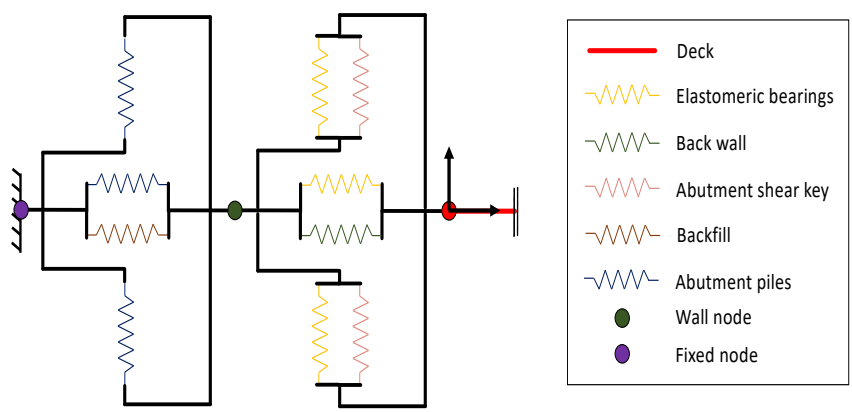

Figure 26. Zero-length element assembly for (a) diaphragm and (b) seat-type abutments.

The translational and torsional masses for column elements were calculated as

$$\begin{aligned} \boldsymbol{M_{xc} = M_{yc} = M_{zc}} &= \boldsymbol{\rho_c A_c L_{\text{trib}}} \\ \boldsymbol{M_{zz}} &= \boldsymbol{\frac{1}{8} \rho_c A_c L_{\text{trib}} D_c} \end{aligned} \tag{32}$$

where L_{trib} and D_c are as defined in Figure 27, and ρ_c and A_c are concrete density and column cross-sectional area, respectively.

The translational and torsional masses for deck segments were computed following the relationships

$$\begin{aligned} \boldsymbol{M_{xd} = M_{yd} = M_{zd}} &= \boldsymbol{\rho_c A_w L_{\text{trib}}} \\ \boldsymbol{M_{cc}} &= \boldsymbol{\frac{1}{12}\rho_c A_w L_{\text{trib}} d_w} \end{aligned} \tag{33}$$

where L_{trib} and d_w are as defined in Figure 27, and A_w is the deck cross-sectional area, respectively.

To simulate structural damping, constant viscous damping ratios were sampled from a normal distribution with a mean of 4.5% and a standard deviation of 1.25% after Padgett (*36*). Lower and upper bound damping ratios were set to 2% and 7%, respectively.

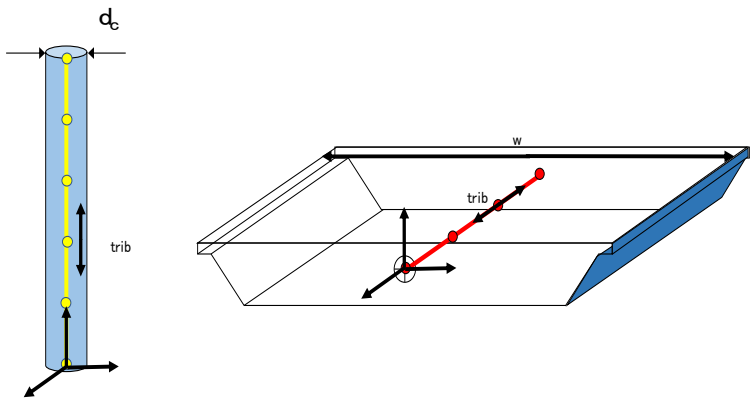

Figure 27. Zero-length element assembly for (a) diaphragm and (b) seat-type abutments.

Filling the gaps: class statistics

Model properties were assigned according to the class statistics suggested by Mangalathu (*17*). Column properties were defined as in Table 2. Colum foundation properties were defined according to Table 3. Properties of elastomeric bearing were prescribed following Table 4. Abutment pile capacities were defined using Table 5. The gap between deck and shear key elements was assumed to follow a uniform distribution with a mean of 0.75 in and a standard deviation of 0.19 in (Lower bound: 0, Upper bound: 1.590).

Table 2. Statistical distributions for lateral abutment pile capacity per deck width.

				Statistical Distribution			
Design Era	Parameter	Units	Type	Mean	SD	Lower Bound	Upper Bound
All	Longitudinal steel reinforcement ratio	N/A	U	2.00	0.33	1.0	3.0
Pre-1971	Concrete compressive strength	ksi	N	3.90	0.48	2.94	5.19
	Steel yield strength	Ksi	N	57.3	4.5	49.0	67.0
	Transverse steel reinforcement ratio	N/A	4 at 12 in. irrespective of the cross-section				
Post-1971	Concrete compressive strength	ksi	N	4.55	0.56	3.43	5.67
	Steel yield strength	ksi	N	69.0	5.5	58.0	80.0
	Transverse steel reinforcement ratio	N/A	U	0.85	0.07	0.4	1.3

Table 3. Statistical distributions for column foundation spring parameters.

Design Era	Bent Type	Foundation Fixity	Statistical Distribution				
			Type	Mean	SD	Lower Bound	Upper Bound
Transverse direction translational stiffness (kip/in)							
Pre-1971	Single	Fixed	LN	1250	2.5	500	3125
	Multiple	Pinned	LN	625	2.5	250	1562.5
	Multiple	Fixed	LN	625	2.5	250	1562.5
1971-1990	Single	Fixed	LN	2000	2.5	500	3125
	Multiple	Pinned	LN	1000	2.5	250	1562.5
	Multiple	Fixed	LN	1000	2.5	250	1562.5
Post-1990	Single	Fixed	LN	2500	2.5	1000	6250
	Multiple	Pinned	LN	1000	2.5	400	2500
	Multiple	Fixed	LN	1000	2.5	400	2500
Longitudinal direction translational stiffness (kip/in)							
Pre-1971	Single	Fixed	LN	1.0	1.0	1.0	1.0
	Multiple	Pinned	LN	1.0	1.0	1.0	1.0
	Multiple	Fixed	LN	1.0	1.0	1.0	1.0
1971-1990	Single	Fixed	LN	1.0	1.0	1.0	1.0
	Multiple	Pinned	LN	1.0	1.0	1.0	1.0
	Multiple	Fixed	LN	1.0	1.0	1.0	1.0
Post-1990	Single	Fixed	LN	1.0	1.0	1.0	1.0
	Multiple	Pinned	LN	1.0	1.0	1.0	1.0
	Multiple	Fixed	LN	1.0	1.0	1.0	1.0
Transverse direction rotational stiffness ($\times 10^6$ kip-in/rad)							
Pre-1971	Single	Fixed	LN	25.0	2.5	10	62.5
	Multiple	Pinned	LN	2.5	2.5	1.0	6.3
	Multiple	Fixed	LN	4.0	2.5	1.6	10.0
1971-1990	Single	Fixed	LN	80.0	2.5	32.0	200.0
	Multiple	Pinned	LN	12.0	2.5	4.8	30.0
	Multiple	Fixed	LN	18.0	2.5	7.2	15.0
Post-1990	Single	Fixed	LN	190.0	2.5	76.0	475.0
	Multiple	Pinned	LN	20.0	2.5	8.0	50.0
	Multiple	Fixed	LN	30.0	2.5	12.0	75.0
Longitudinal direction rotational stiffness ($\times 10^6$ kip-in/rad)							
Pre-1971	Single	Fixed	LN	1.5	1.5	1.00	2.25
	Multiple	Pinned	LN	1.0	1.5	0.67	1.50
	Multiple	Fixed	LN	1.0	1.5	0.67	1.50
1971-1990	Single	Fixed	LN	1.0	1.0	1.0	2.25
	Multiple	Pinned	LN	1.0	1.0	0.67	1.50
	Multiple	Fixed	LN	1.0	1.0	0.67	1.50
Post-1990	Single	Fixed	LN	1.0	1.0	1.00	1.32
	Multiple	Pinned	LN	1.0	1.0	0.96	1.50
	Multiple	Fixed	LN	1.0	1.0	0.96	1.50

Table 4. Statistical distributions for elastomeric bearing parameters

Design Era	Parameter	Units	Statistical Distribution				
			Type	Mean	SD	Lower Bound	Upper Bound
Pre-1971	Stiffness / deck width	kip/in/ft	LN	0.40	0.35	0.70	3.0
	Coefficient of friction	-	N	0.30	0.10	0.10	0.5
1971-1990	Stiffness / deck width	kip/in/ft	LN	0.77	0.52	0.70	6.0
	Coefficient of friction	-	N	0.30	0.10	0.10	0.5
Post-1990	Stiffness / deck width	kip/in/ft	LN	0.00	0.45	0.40	2.5
	Coefficient of friction	-	N	0.30	0.10	0.10	0.5

Table 5. Component demand threshold (CDT) values used in computing fragility functions.

Abutment type	Units	Statistical Distribution				
		Type	Mean	SD	Lower Bound	Upper Bound
Diaphragm	kip/ft	LN	1.79	0.35	2.5	12.0
Seat	kip/ft	LN	2.08	0.35	4.0	16.0

Table 6. Statistical distributions for lateral abutment pile capacity per deck width.

Component	EDP	Units	$M_{\text{CDT-0}}$	$M_{\text{CDT-1}}$	$M_{\text{CDT-2}}$	$M_{\text{CDT-3}}$
		Columns				
Pre-1971	Curvature ductility	-	0.40	0.35	0.70	3.0
1971-1990	Curvature ductility	-				
Post-1990	Curvature ductility	-	0.30	0.10	0.10	0.5
		Abutment Seat				
AS1-S	Displacement	inches	0.5	1.0	2.0	3.0
AS2-S	Displacement	inches	0.5	1.0	2.0	3.0
AS3-S	Displacement	inches	0.5	1.0	2.0	3.0
AS3-L	Displacement	inches	0.5	1.0	2.0	3.0
AS4-S	Displacement	inches	0.5	1.0	2.0	3.0
AS4-L	Displacement	inches	0.5	1.0	2.0	3.0
		Abutment Deformation				
Passive	Displacement	inches	3.0	10.0	-	-
Active	Displacement	inches	1.5	4.0	-	-
Transverse	Displacement	inches	1.0	4.0	-	-
		Joint Seal				
Type A	Displacement	Inches	0.5	-	-	-
Type B	Displacement	Inches	1.0	-	-	-
Strip	Displacement	Inches	2.0	5.0	-	-
Modular	Displacement	Inches	4.0	10.0	-	-
Bearings	Displacement	Inches	1.0	4.0	-	-
Restrainers	Displacement	Inches	1.5	4.0	-	-
Shear keys	Displacement	Inches	1.5	5.0	-	-
Deck	Displacement	Inches	4.0	12.0	-	-
		Bent Foundation				
Translation	Displacement	Inches	1.0	4.0	-	-

Rotation	Rotation	Radians	4.0	6.0	-	-

Bridge-specific fragility functions

Component demand thresholds required to compute the fragility function for each damage class is defined according to Ramanathan et al. (*39*). Dispersion value for all components and CDT levels are assumed 0.35. For abutment seat classification method please refer to the referenced paper.

Metadata extraction and estimation from images and rules

At the highest level, the image-based modeling framework consists of five steps:

1. Automated identification of bridge location
2. Semi-automated development of bridge wireframe model
3. Semi-automated determination of deck properties
4. Automated extraction of column geometries
5. Semi-automated determination of in-span hinge properties

These key steps are described in further detail in the following sections, wherein various steps are infused with rules extracted from various guideline documents to estimate metadata that cannot be extracted from images. After providing an overview of the aforementioned steps, the overall method is appraised through a validation study that compares the characteristics of a specific bridge model against a structural model of the same bridge established using as-built drawings.

Identifying the bridge location and centerline curve

The framework is capable of automatically identifying bridge locations based on the approximate coordinate information available in the National Bridge Inventory (NBI) (*37*). The program first sends a query through OpenStreetMap's Overpass API (*38*) and searches for all the bridges fully or partially covered within a circle of a mile-radius centered at the NBI coordinates of the considered bridge. It then reads the route information of all the bridges selected through the query and keeps the one(s) that match this information. Then, the program randomly samples two points along the centerline curves of each of the selected bridges and cross-checks both the route and direction information of the selected bridges. At this step, the results are narrowed down to a single match, and the centerline information necessary for wireframe model construction is established. Figure 28 summarizes the described bridge location and centerline identification procedure.

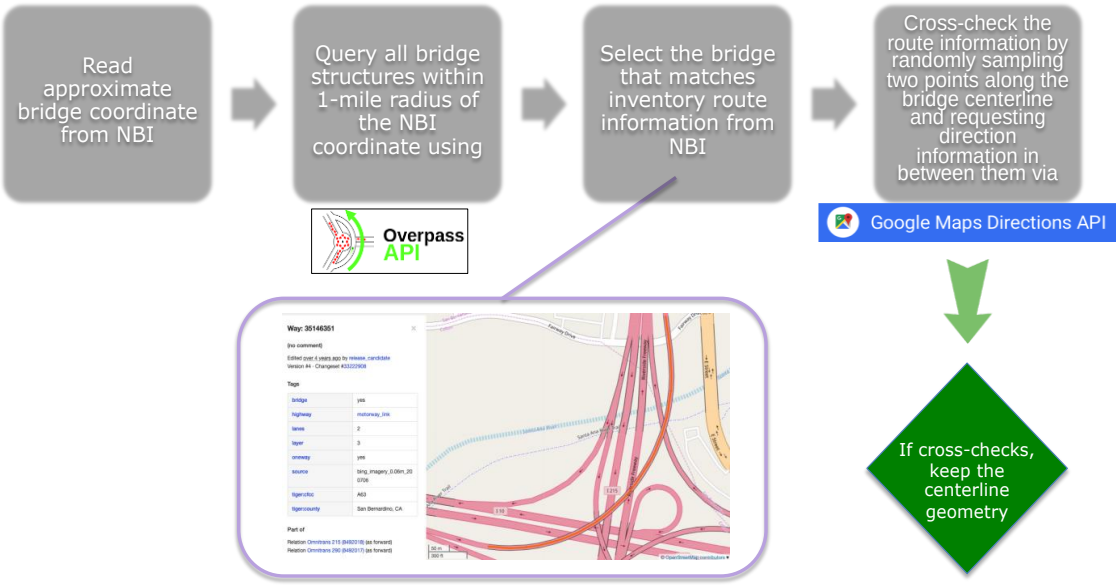

Figure 28. Bridge location and centerline identification.

Developing a wireframe model

Developing the bridge wireframe model requires identification of ground surface level, pier locations, and the distance from the ground surface to the top of the deck. The framework captures ground elevations by automatically creating a minimum of 1000 sampling points along the bridge centerline curve, then querying ground elevations at those points via Google Maps Elevation API. Determining pier locations and the normal between the ground surface and deck top surface is somewhat more involved. First, two lines (curves rather) of virtual cameras are created offset from the bridge centerline by a distance proportional to the length of the bridge, and all Google Street View images along this line are harvested. Then images are semantically segmented so that all areas belonging to column and deck elements are clearly marked. Next, based on their order of occurrence along the centerline, each column element is assigned a number. Then images including each column element are placed in separate batches, and by performing auto-calibration, camera parameters for the images are determined. Next, column bottom edges and deck's top edges are detected and the length of the normal line that links these two edges is measured for each column. Last, a camera image fully aligned with the bridge is selected, its principal vertical plane is marked on the image, and the shortest distance between the plane and the columns in the image are measured to obtain the column locations. This last step is repeated until all column locations are determined. Even if this process requires minimal user interruption, it is not fully automated due to occasional inaccuracies in semantic segmentation and edge detection procedures. Figure 29 summarizes the wireframe model development procedure.

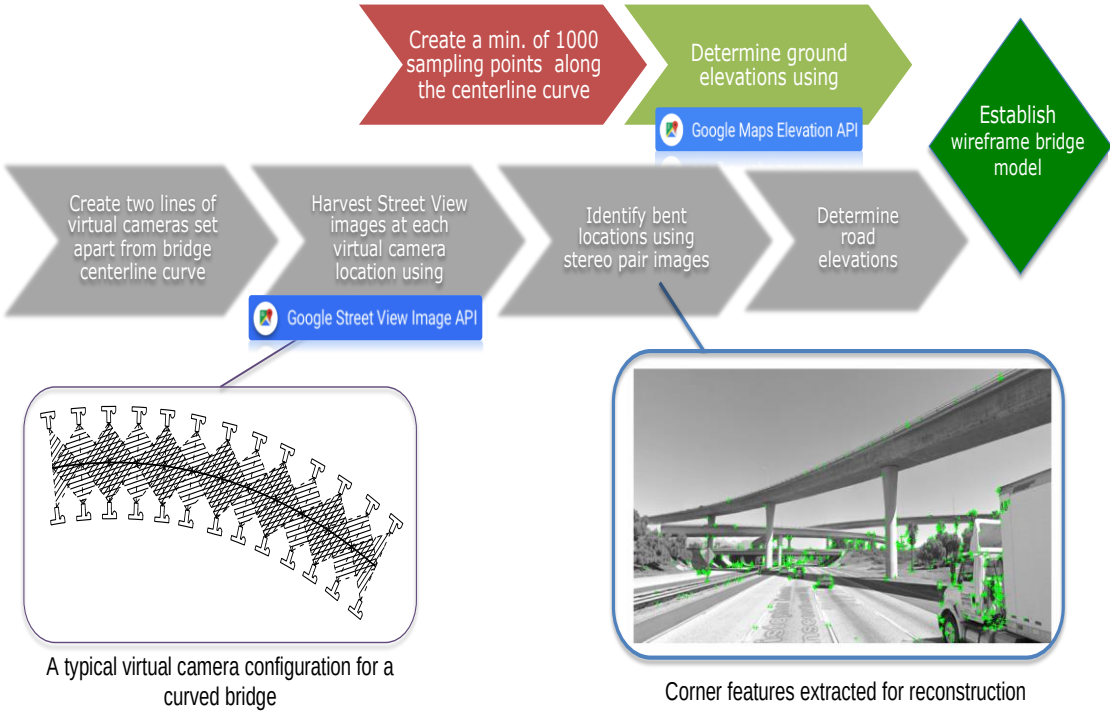

Figure 29. Developing the bridge wireframe model.

Determining the deck properties

The primary assumption in defining the deck is that it remains elastic under earthquake shaking. Hence, as long as a valid estimation of the gross area of the deck can be made, the geometric properties extracted from Street View images shall be sufficient. Deck reconstruction starts with reading the deck metadata fields from NBI. One of the NBI fields gives the top width of the bridge deck. The bottom width of the deck is extracted from auto-calibrated images from the previous step. Then the horizontal alignment of the deck is extracted by automatic lookup of AASHTO code for the design year of the bridge and back-calculated based on the posted speed limit for the bridge (obtained from Google Directions API). Figure 30 and Figure 31 summarize the deck reconstruction process.

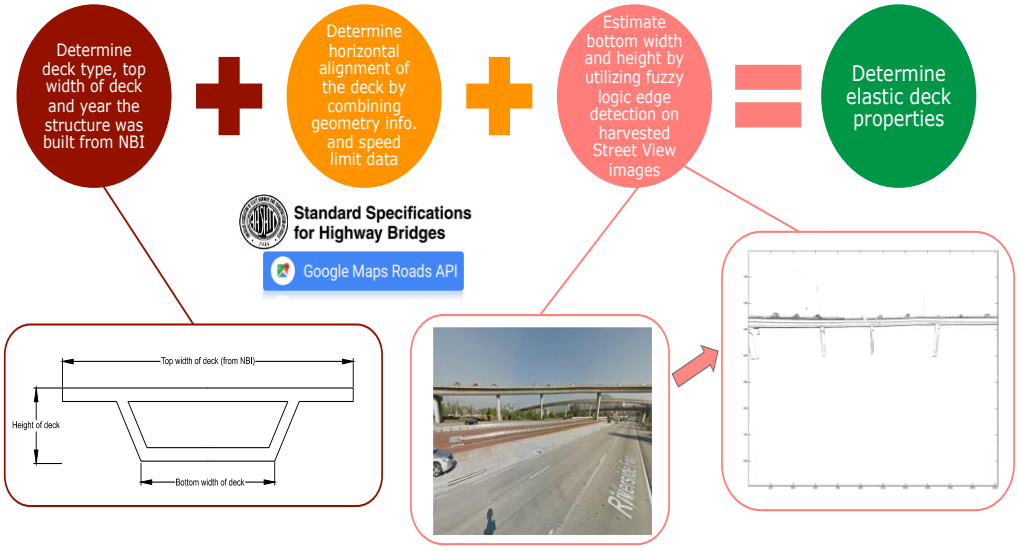

Figure 30. Determination of deck properties: general procedure.

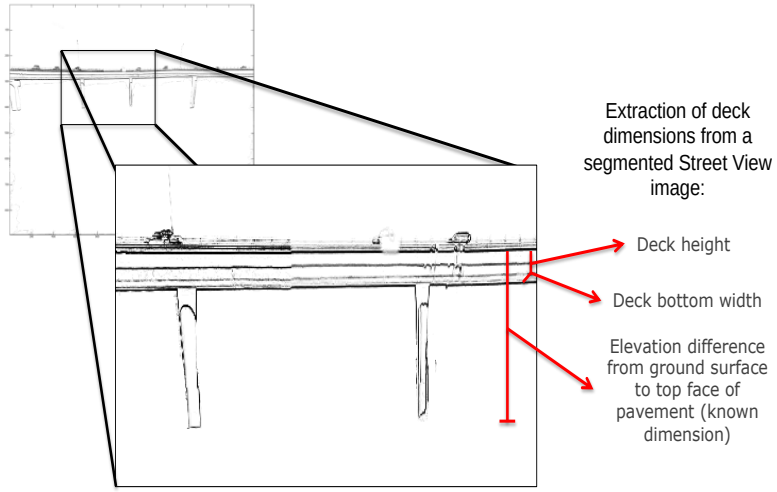

Figure 31. Determination of deck properties: closeup.

Determining the column properties

The automated extraction of column geometries consists of three primary steps. First, an edge detection algorithm is executed on segmented column patches, and the number of edges is counted (e.g., two edges if circular, three edges if rectangular). Then column heights and widths are sampled at numerous intervals to determine the column dimensions. Then using class statistics for bridge columns (*17*), longitudinal and transverse rebar locations are calculated. Figure 32 summarizes the process for extracting column shape and dimensions.

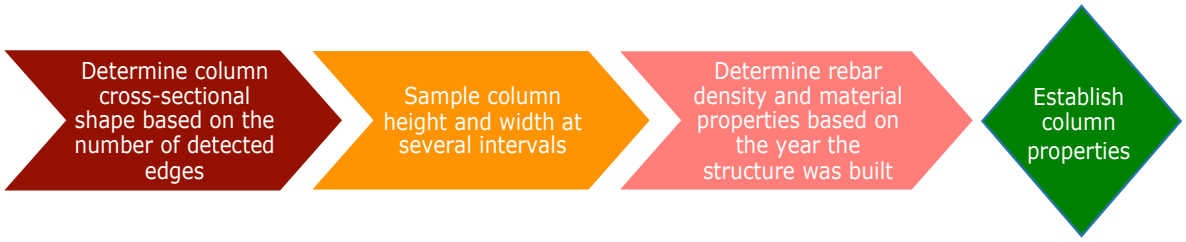

Figure 32. Automated extraction of column properties.

Determining the in-span hinge properties

The determination of in-span hinge locations is performed identically to column location determination. The main difference is the difficulty in determining the location and gap size. Segmented patches for the deck are evaluated with a gradient change detector for location identification. However, the filter is not flawless, so seldom user interruption is required.

Validation study: Colton interchange bridge

A structural model of the Interstate-10E/Interstate-210N interchange bridge (also known as the Colton interchange bridge) was developed based on the as-built drawings, and several geometric and structural characteristics were compared against its image-based model. Figure 33 through Figure 34 display the intermediate steps of image-based modeling process as well as the final model.

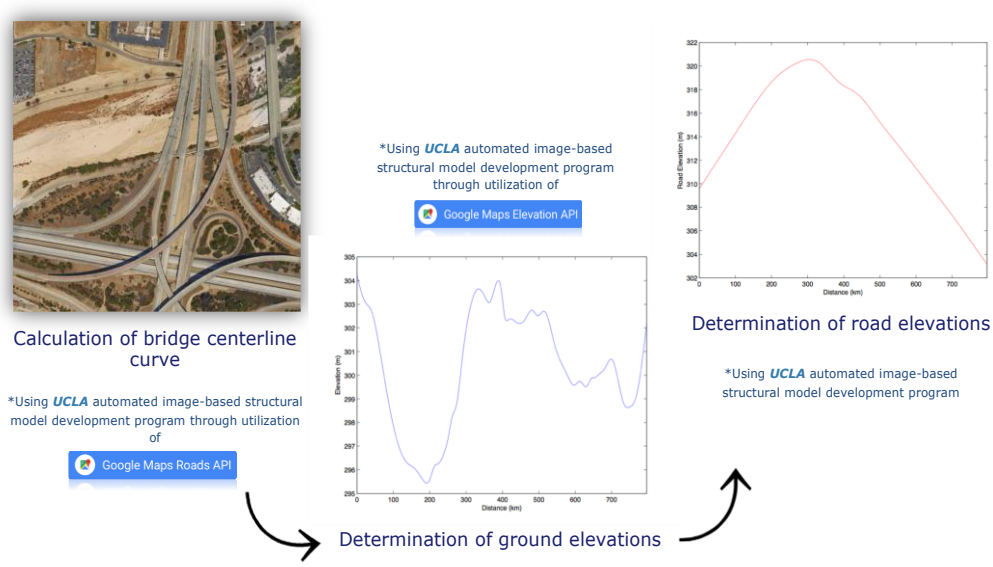

Figure 33. Colton Interchange: determination of centerline, ground and deck elevation.

Identification of bent locations

*Using ***UCLA*** automated image-based structural model development program via *Image Analyzer Module*

*Using ***UCLA*** automated image-based structural model development program via *Wireframe Model Builder Module*

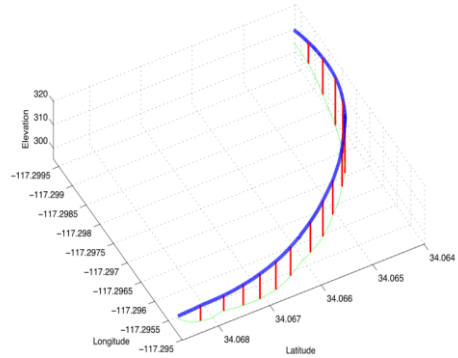

Establishing of wireframe model

Figure 34. Colton interchange: identification of column locations, and the resulting wireframe model.

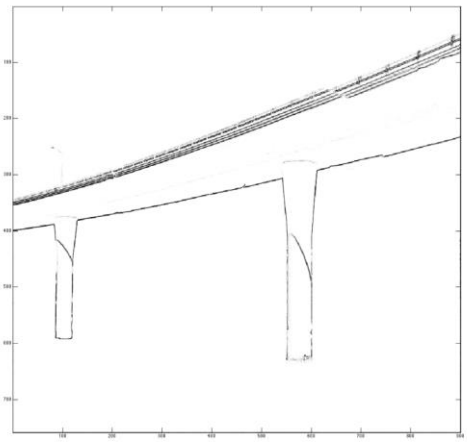

Detection of column edges

*Using ***UCLA*** automated image-based structural model development program via *Fuzzy Logic Edge Detection Module*

*Using ***UCLA*** automated image-based structural model development program via *Pixel Counter Module*

Determination of column dimensions

Figure 35. Colton interchange: column edge detection and dimension extraction.

Figure 36. Colton interchange: identification of in-span hinge locations.

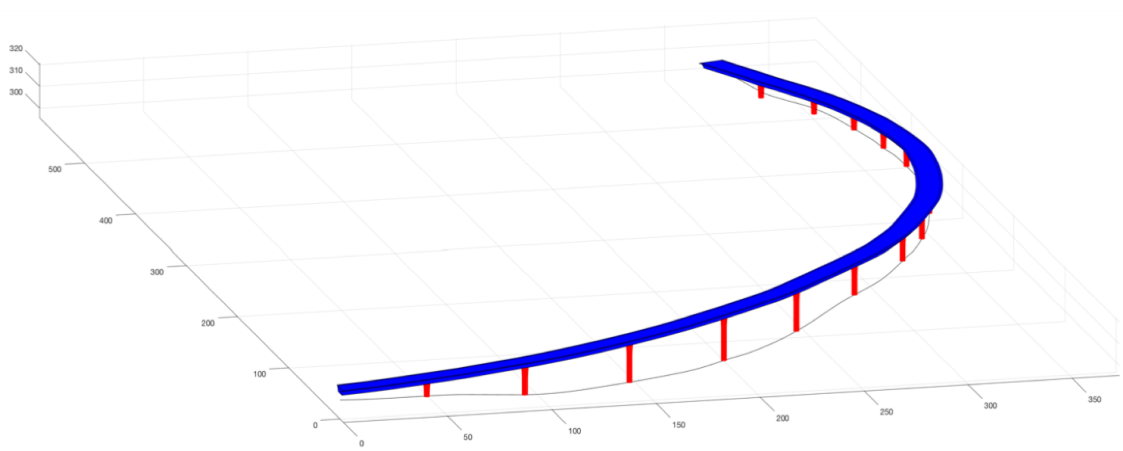

Figure 37. Colton interchange: full three-dimensional model.

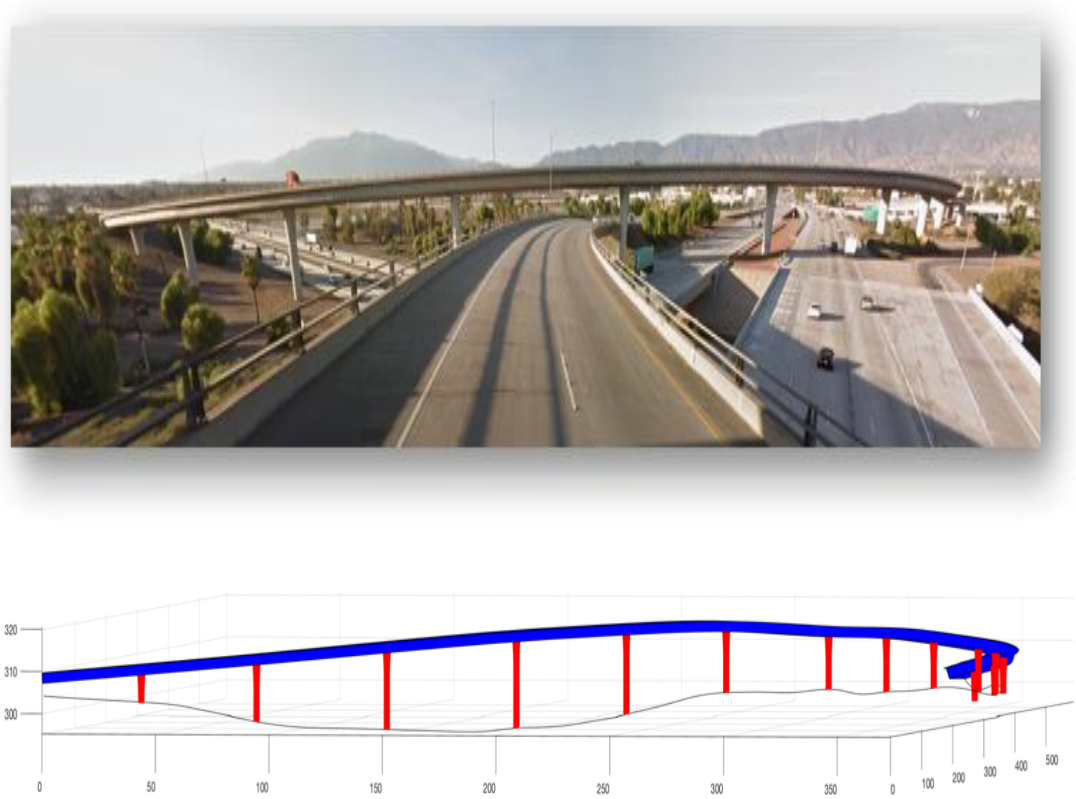

Figure 38. Colton interchange: Full 3-D Model visual comparison against Street View image.

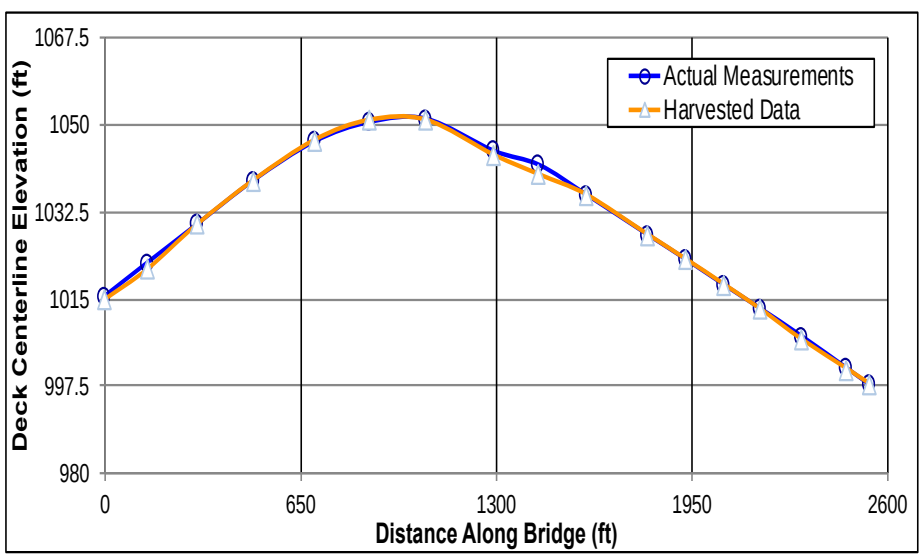

Figure 39. Colton interchange: image-based vs. as-built deck elevation.

Figure 35 through Figure 36 compare the geometric features of the image-based model vs. the as-built model. Table 7 makes a comparison between the modal periods and Figure 42 compares collapse fragilities of the image-based model vs. the as-built model. As evident from the results, image-based

results almost perfectly match the as-built geometry and closely approximates the as-built structural behavior.

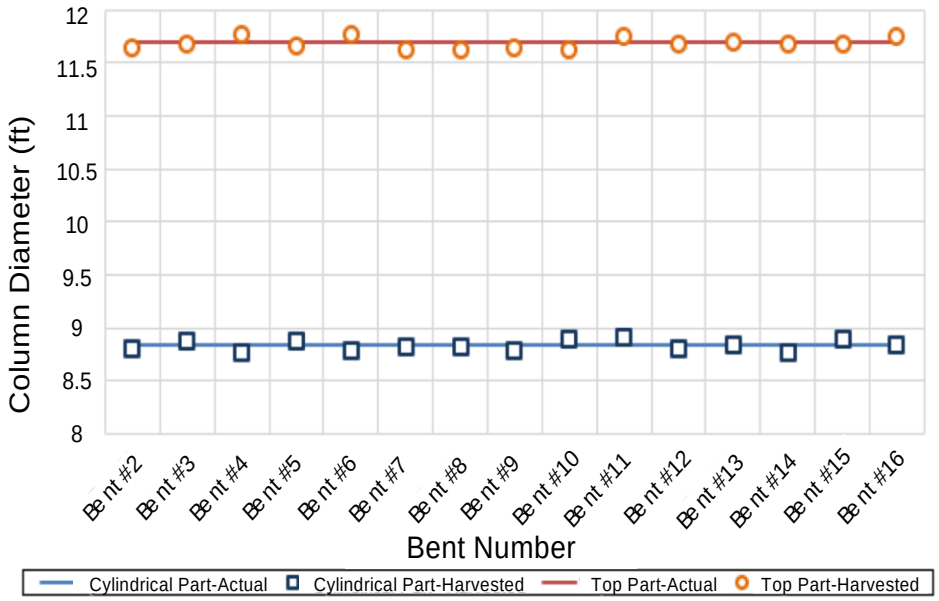

Figure 40. Colton interchange: image-based vs. as-built column diameters.

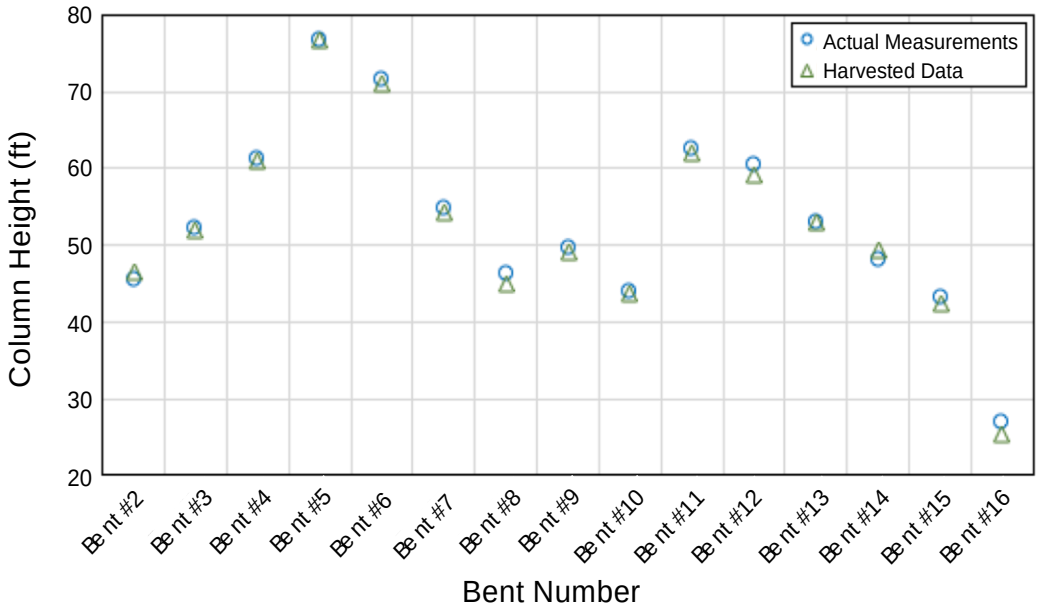

Figure 41. Colton interchange: image-based vs. as-built column heights.

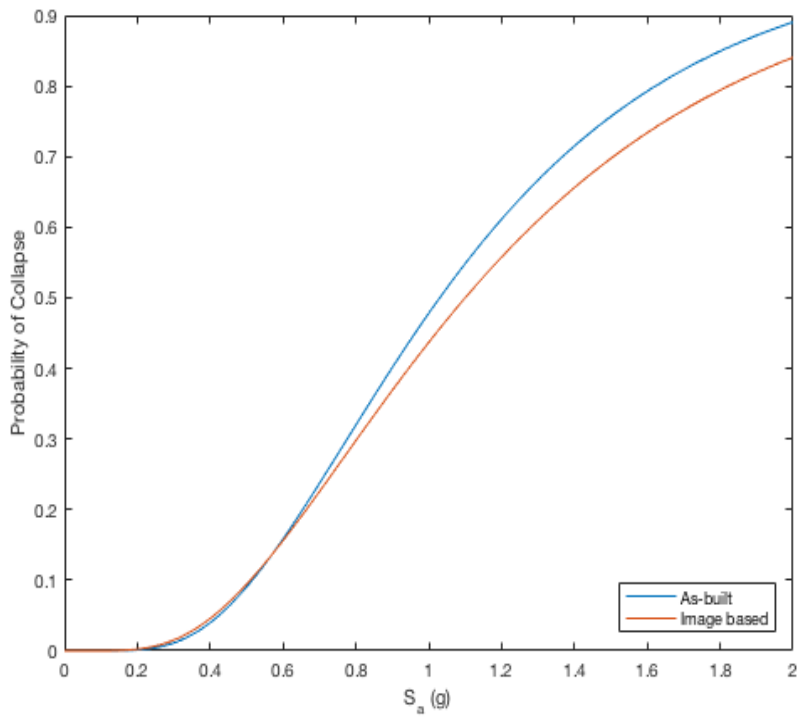

Figure 42. Colton interchange: image-based vs. as-built collapse fragility functions.

Table 7. Image-based versus as-built: Modal Periods

$T_{\text{image-based}}$	$T_{\text{as-built}}$
1.36	1.53
1.18	1.29
1.03	1.09
0.95	1.02
0.89	0.94
0.84	0.88
0.78	0.80
0.75	0.79

Putting it all Together: BridgeR Workflow

The aforementioned modeling capabilities are appended with regional infrastructure seismic damage assessment (which includes hazard characterization), transportation network analysis, and economic impact analysis capabilities and combined into a single workflow. This four-part workflow to assess the vulnerability and resilience of a transportation network in the event of an earthquake is henceforth referred to as **BridgeR**, and its flowchart is shown in Figure 43. In this section, we detail the latter three steps of infrastructure assessment, transportation network analysis, and economic impact analysis.

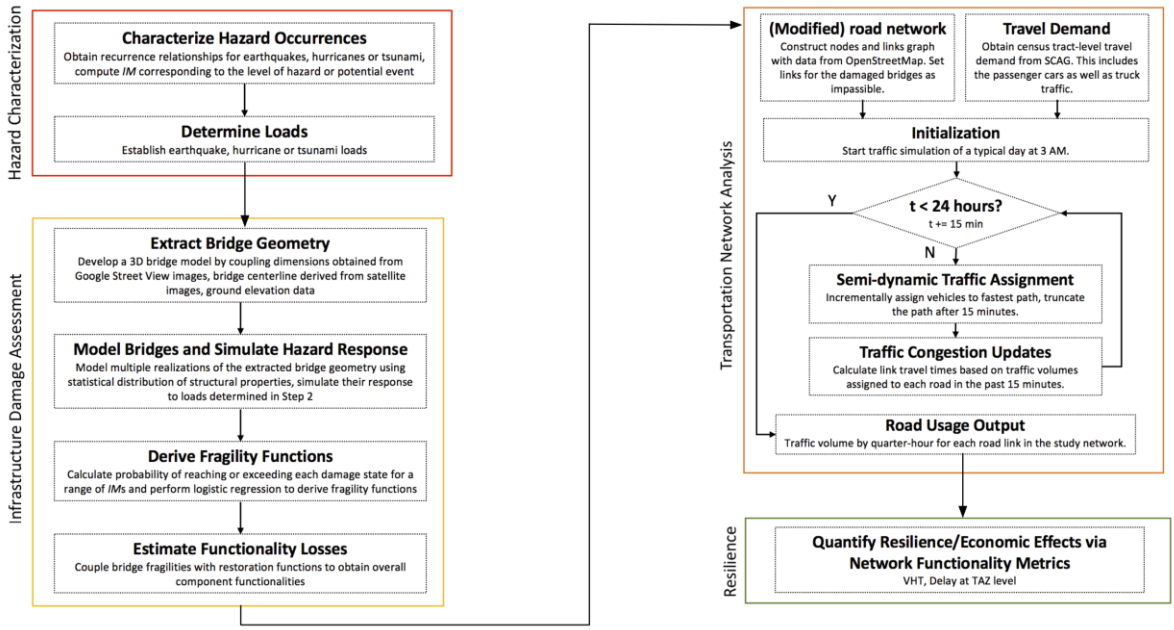

Figure 43. BridgeR flowchart.

Infrastructure damage assessment

Infrastructure damage assessment requires generating model inventories, but additionally requires characterization of hazard and the resulting structural damage. The combined effort requires five high-level steps:

1. Identifying tentative bridge locations for a region from National Bridge Inventory and refining this location information using OpenStreetMap and routing APIs,
2. Downloading all street-level imagery that views each detected bridge,
3. Reconstructing three-dimensional bridge geometry for each bridge using downloaded imagery,
4. Populating these geometric shells with structural information using class statistics to develop nonlinear bridge models,
5. Calculating bridge fragility functions using component damage thresholds available in the existing literature.

The first step, identifying bridge locations and centerline geometry, begins with extracting approximate coordinate information available in the National Bridge Inventory (NBI) (*37*). Once these coordinate values are obtained, all bridge centerlines that are within a mile radius of NBI coordinates are detected using OpenStreetMap (OSM)'s Overpass API (*38*) and the bridge geometries that match the route information stated in NBI are retained. Subsequently, to narrow down the query to a single unique matching centerline, a navigation query from the beginning and end vertices of each centerline curve is generated using Google Directions API, and the route/direction information for a bridge centerline that match NBI route and direction information is selected.

Benefiting from the unique strengths of each data source, this process results in accurate centerline extractions. NBI contains precise location and route information for every bridge in the US but lacks the

centerline information captured in OSM. OSM, on the other hand, has accurate centerline polygon and route information based on the US Census Bureau TIGER/Line roadway polygons (*39*) but lacks the direction information needed, e.g., northbound or southbound, to match these polygons to NBI bridges. Direction API provides detailed direction information between two points but is somewhat limited in the accuracy of the path connecting these points. By combining these three sources, the centerline geometry of a bridge and the facility it carries is easily identified.

To download the street-level images for each bridge, two curves offset from the bridge centerline by a distance proportional to the NBI length of the bridge are computed. Next, all the Google Street View imagery on or near these curves are harvested keeping track of the camera locations of images as they are obtained.

The street-level imagery for each bridge is semantically segmented using a deep learning model utilizing DeepLabV3-ResNet101 architecture (*40*) to identify all image regions containing bridge bent and deck elements. Then, the unique columns in each image and their locations are determined based on their order of occurrence and their linear distance along or offset from the bridge centerline. At this step, images for each unique column are grouped separately to determine column dimensions. By running the end-to-end wireframe parsing model by Zhou et al. (*41*) on column masks of segmented images, the vertical column lines are identified; counting the number of these vertical edges, column shapes are determined (e.g., two edges if circular, three edges if rectangular). Camera parameters at each column location are extracted using the multi-view automatic calibration pipeline developed by Vasconcelos et al.(*42*). Subsequently, the heights and widths of each column are sampled at numerous intervals to determine the column dimensions. Superstructure depth is measured as the normal distance between the bottom and top faces of the superstructure. The top width of the bridge deck is read from the relevant NBI field, and the bottom is extracted from auto-calibrated images.

By the end of this step, a three-dimensional geometric model for each bridge is established. To convert these geometric models into structural models, the class statistics by Mangalathu (*17*) are utilized. For example, for bridge columns longitudinal and transverse rebar locations are computed based on the era-specific rebar ratios (where construction year of a bridge is attained from NBI). Whereas, the superstructure is assumed to remain elastic under earthquake shaking. Hence, elastic properties based on gross area of the superstructure are assigned to line elements representing the superstructure.

The relationship between probability for each bridge to reach or exceed different damage states and ground shaking intensity measure (IM) 1-second spectral acceleration are defined using fragility functions. Fragility functions are prescribed as log normally-distributed functions and were generated for five distinct damage states: no damage (ds_1), slight (ds_2), moderate (ds_3), extensive (ds_4), and complete (ds_5). Each fragility function corresponds to one of these damage states and is characterized by a median value IM (M), and a log-normal standard deviation value (β). The generic form of a fragility function is given by

$$\Pr\left(\boldsymbol{D}^{\boldsymbol{k}} \geq \mathrm{ds}_{\boldsymbol{j}}\right) = \mathbf{1} - \boldsymbol{\Phi}_{\boldsymbol{j}}^{\boldsymbol{k}}\left(\frac{\ln\left(x^{\boldsymbol{k}}/\boldsymbol{M}\right)}{\boldsymbol{\beta}}\right) \tag{34}$$

where k is the index for IMs, j is the index for PBEE damage states, D^k is the damage state of network component due to IM k, Φ is the normal cumulative distribution function, and x^k is the IM k at the site of the network component. Note that the probability of a system being in or exceeding the no damage, ds_1, state is always 1 ($\Pr\left(D^k \geq \mathrm{ds}_1\right) = 1$). The component threshold values required to develop these fragility curves were defined as outlined by Ramanthan et al. (*43*).

Translation between bridge fragilities and downtime is performed by calculating the probability of network components being in one of the five damage states, and aggregating these probability measures to restoration functions that correspond to individual damage states. Open literature on restoration functions is particularly limited, and the restoration functions published by FEMA (*15*) are the main tool used for tying component damage information to downtime estimates. For a set of IMs, the probability of a network component being in a damage state (P_j^k) is calculated as

$$\mathrm{P}_j^k = \begin{cases} \Pr\left(\boldsymbol{D^k} \geq \mathrm{ds}_j\right) - \Pr\left(\boldsymbol{D^k} \geq \mathrm{ds}_{j+1}\right) & \boldsymbol{j = 1, 2, 3, 4} \\ \Pr\left(\boldsymbol{D^k} \geq \mathrm{ds}_5\right) & \boldsymbol{j = 5} \end{cases} \tag{35}$$

For a set of IMs, expected downtime ($\mathrm{E}[D^k]$) is defined with respect to P_j^k as in

$$\mathrm{E}\left[\boldsymbol{D^k}\right] = \sum_{\boldsymbol{j=1}}^{\boldsymbol{5}} \mathrm{P}_j^k \cdot \boldsymbol{RC_j} \tag{36}$$

where RC_j is the recovery function corresponding to the damage state denoted by index j.

Transportation

Given the network supply and travel demand inputs, the traffic assignment module is then initialized: the simulation usually starts at 3 AM, when there is relatively light traffic on the road network. With a time step of 15 minutes, vehicles (time-stamped OD pairs) with a departure time between 3 - 3.15 AM are incrementally assigned an initial fastest path based on free-flow traffic conditions. The incremental assignment here is to increase the stability of the results by avoiding all vehicles getting assigned to the same routes. After each increment, the traffic congestion status is updated for the network and a new travel time is calculated for each link using the Bureau of Public Roads (BPR) volume-delay curves (*46*) as shown in Eq. 37.

$$\boldsymbol{t_i} = \boldsymbol{t0_i} * \left(\boldsymbol{1} + \boldsymbol{\alpha} * \left(\frac{\boldsymbol{v_i}}{\boldsymbol{c_i}}\right)^{\boldsymbol{\beta}}\right) + \text{traffic signal delay} + \text{crossing delay} \tag{37}$$

where t_i is the travel time on link i, $t0_i$ is the free-flow travel time on link i, v_i is the flow on link i, c_i is the capacity of link i, and α and β are calibration parameters parameters set to 0.6 and 4 respectively. Traffic signal and crossing delays are also considered as this information is also provided by OSMnx.

An intermediate stopping location is determined for each vehicle that cannot finish the journey within the 15-minute interval. The intermediate stopping locations will then be set as the new origin to allow vehicles to finish the journey in the subsequent time steps. Such incremental assignment and residual demand calculation procedures are repeated for each 15-minute interval until 3 AM the next day. The outputs include both vehicle-level information (travel time) and link-level information (traffic volume per 15-minute interval). Many summary statistics, such as the Vehicle Miles Traveled (VMT) and Vehicle Hours Traveled (VHT) can thus be derived from this output.

The traffic model has been adapted here to capture the effects of bridge damages. Specifically, for damaged bridges (and surrounding or underlying roads that cannot be accessed), the traffic model will label them as “closed links". For these closed links, they are assigned extremely small speed limit and capacity, which effectively leads to extremely high travel times (e.g., over 10 hours) for vehicles using them. In the simulation code, a supplementary logic is implemented to check the travel time of each assigned route. If the route travel time is over a certain threshold, the route must have gone through one

of the closed links and no faster path exists. The trip is then labeled as “unfulfilled". It is expected that more trips will be unfulfilled with increasing bridge damage severity.

If additional information such as different trip activities and different vehicle types are available, each agent can be labeled and restricted accordingly in the simulation for a richer analysis later on.

Economic impact estimation

The economic cost of damages in a transportation network can be split into two components: direct costs and indirect costs as shown (*3*)

$$\boldsymbol{C} = \boldsymbol{C_{direct}} + \boldsymbol{C_{indirect}}. \tag{38}$$

Direct costs associated with bridge b are computed based on the amount of resources needed to repair the damaged road components in the network as shown in

$$\boldsymbol{C_{direct}} = \sum_{\boldsymbol{b=1}}^{\boldsymbol{B}} \boldsymbol{C_{direct}^{(b)}} \tag{39}$$

$$\boldsymbol{C_{direct}^{(b)}} = \mathbb{I}^{(\boldsymbol{b})} \times \mathbf{RCR} \times \boldsymbol{A_b} \times \mathbf{unit\ normal\ cost} \tag{40}$$

where RCR is the repair cost ratio and A_b is the area of the bridge b (*47*). The unit replacement cost is $3154 per square meter (*37*). On the other hand, indirect costs incurred over the time period when road components are damaged can be further split into two components: costs due to delays and costs due to lost demand or unfulfilled trips as shown in

$$\begin{aligned} \boldsymbol{C_{indirect}} &= \boldsymbol{C_{delays}} + \boldsymbol{C_{connectivity}} \\ &= \boldsymbol{\alpha \Delta T} + \boldsymbol{\gamma U} \end{aligned} \tag{41}$$

where α is the value of travel time and γ is the value of productivity. ΔT is the change in total travel time and U is the number of unfulfilled trips, both relative to the base pre-earthquake scenario. α and γ vary for each region and can be computed using

$$\begin{aligned} \boldsymbol{\alpha} &= \frac{\text{median household income, USD}}{\text{2080 hours worked per year}}, \\ \boldsymbol{\gamma} &= \frac{\text{Annual gross regional product}}{\text{Annual labor hours}}. \end{aligned} \tag{42}$$

Once cost estimates are obtained, they can be compared with other economic measures such as the gross domestic product (GDP) of the area to get a sense of its scale compared to the economy at large.

Case Study: Ports of Los Angeles and Long Beach

Hazard Characterization and Damage Assessment

Nonlinear structural models were developed for 1,000 bridges around the Ports of Los Angeles and Long Beach (POLA/POLB) using an automated image-based approach. The expected 1-second spectral accelerations at each bridge site were obtained using the physics-based approach proposed by Southern California Earthquake Center (*48*) for a M_w 7.4 Palos Verdes Fault scenario event, two miles off the port islands. Expected damage probabilities and functionality levels, together with the required recovery time of the bridges, were determined based on computed 1-second spectral accelerations. Figure 44 shows the

fragility functions computed for two of the bridges modeled for this study. Figure 45 shows the damage map predictions using the proposed method. This damage map is extended into a road closure map as shown in Figure 46 with the expectation that surrounding segments of damage bridges will also be closed due to inspection. In this road closure map, 59 miles of roadway were predicted to be closed the day after the scenario earthquake, 44 miles of roadway remained closed 3 days post-earthquake, 14 miles of roadway remained closed 7 days post-earthquake, 10 miles of roadway remained closed 14 days post-earthquake, and 6 miles of roadway remained closed 30 days post-earthquake. This road closure map is used as the input to the subsequent transportation network analysis.

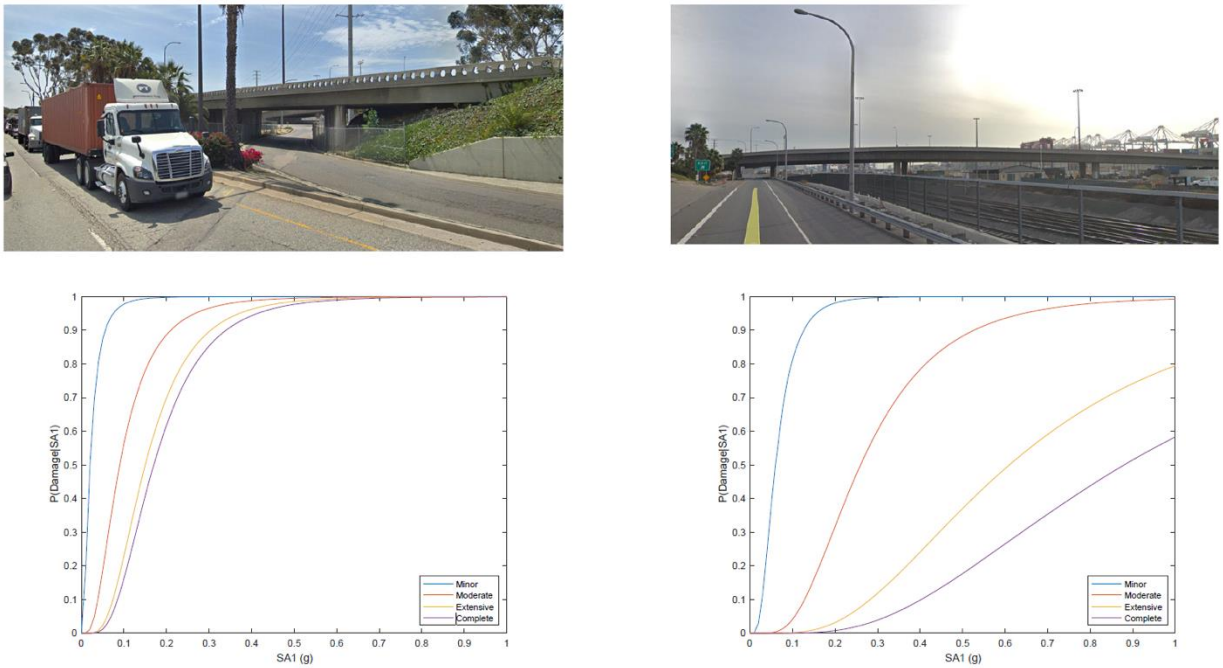

Figure 44. Fragility functions computed for two of the modeled bridges.

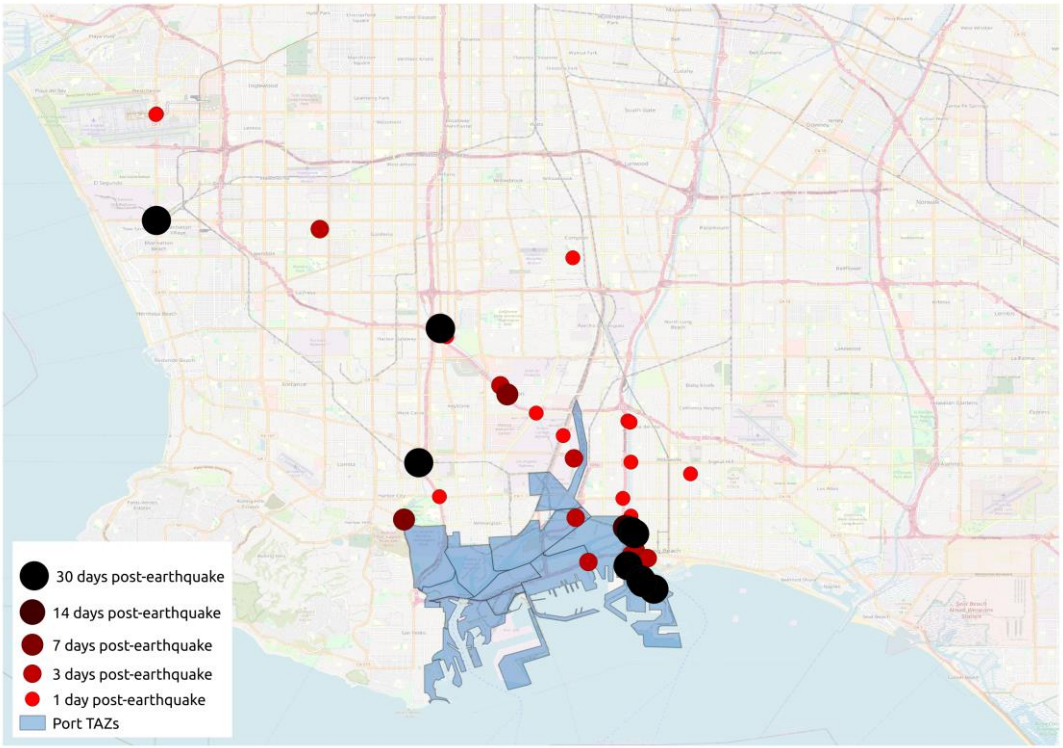

Figure 45. Damage map.

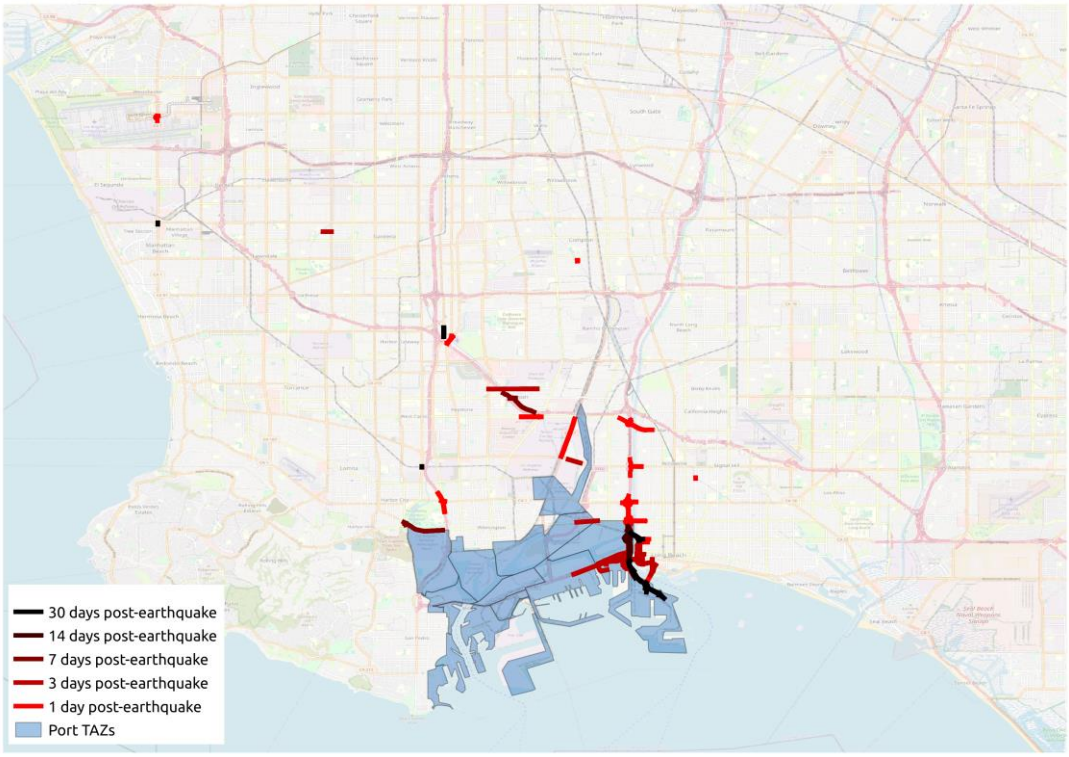

Figure 46. Road closure map.

Transportation Network Analysis

Road network data

Road network data for six counties in Southern California represented by the Southern California Association of Governments (SCAG) has been gathered from OSMnx. The network is converted into a graph representation consisting of 1,444,790 edges and 615,174 nodes where each edge represents a road segment and each node represents a road connection or intersection.

Travel demand data

Inter-traffic analysis zone (TAZ) origin-destination data in normal situations (i.e., without earthquake damage) was also obtained from SCAG. Processing this data led to a total of 42,056,426 trips in the whole SCAG region for a typical day composed of 40,814,733 car trips and 1,241,693 truck trips. Table 8 shows the travel demand summary for each time of day, while Figure 47 and Figure 48 show visualization of the overall travel demand and the port travel demand.

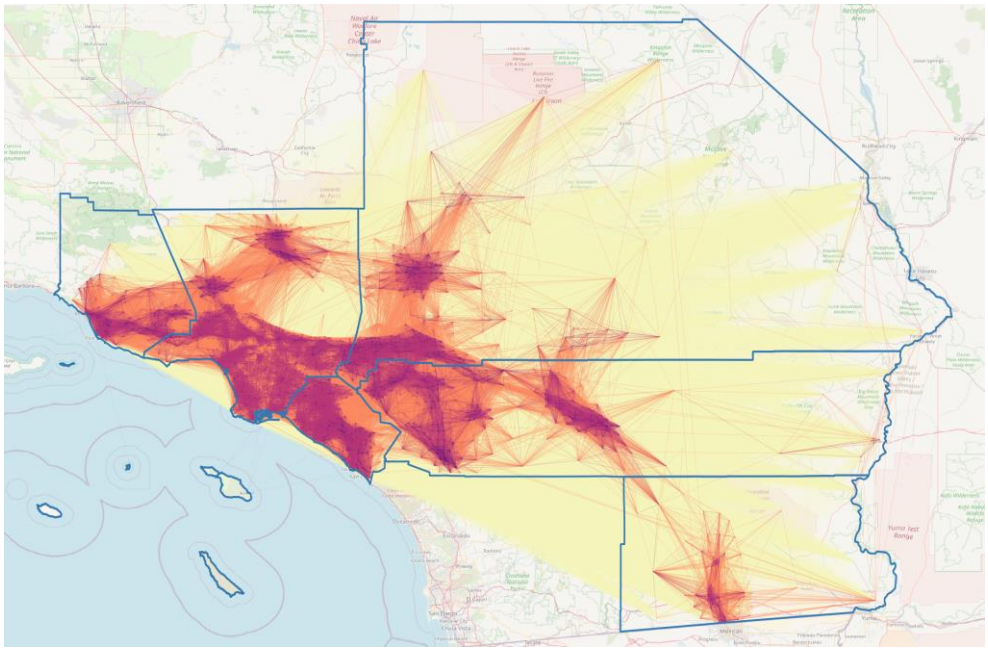

Figure 47. Overall travel demand.

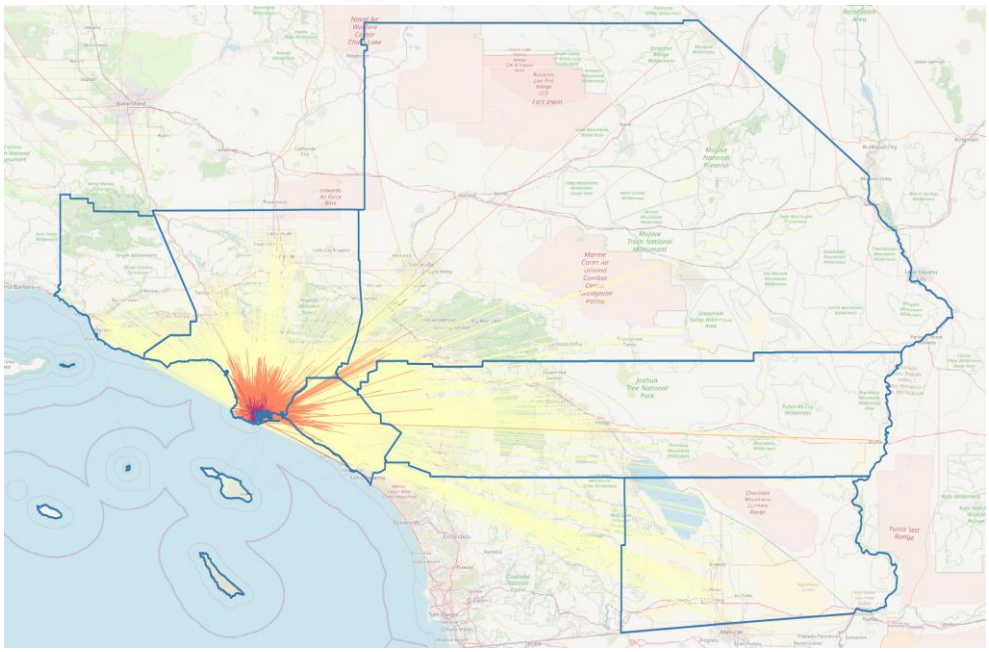

Figure 48. Port travel demand.

Table 8. Travel demand summary.

Time of day	No. of car trips	No. of truck trips	Total trips
6am - 9am	5,202,331	48,248	5,250,579
9am - 3pm	12,346,440	166,006	12,512,446
3pm - 7pm	9,241,983	51,815	9,293,798
7pm - 9pm	3,117,935	69,886	3,187,821
9pm - 6am	1,674,401	55,999	1,730,400

While Khademi et al. (*49*) suggest that travel demand substantially changes post-earthquake and employed hundreds of person-hours of experts to determine the new travel demand, it is difficult to do this for most places. Herein, we use the same travel demand pre- and post-earthquake, but we anticipate that a number of trips will not be completed in the post-earthquake simulation scenarios due to lack of connectivity in the network.

Due to the computationally intensive requirements of this kind of traffic simulation, we decided to sample the origin-destination data such that 1 agent represents 5 vehicles. The final simulation input is composed of 8,158,000 car agents and 246,218 truck agents for a total of 8,404,218 agents. The output figures are also adjusted accordingly with a factor of 5.

Traffic simulation

A Python-based traffic assignment module, which computes sub-hourly changes in road usage through an interactive assignment process with residual demand, was used. Each trip is assigned an initial route based on the computed shortest path using contraction hierarchies from origin to destination (*50*). Each edge's volume is updated every 15 minutes and each trip's shortest path is recomputed based on the new network congestion status. Trucks were restricted from traveling on residential roads.

Six scenarios were simulated: (1) a base scenario with no road closures, (2) a scenario one-day post-earthquake, (3) a scenario 3 days post-earthquake, (4) a scenario 7 days post-earthquake, (5) a scenario 14 days post-earthquake, and (6) a scenario 30-days post-earthquake. Each post-earthquake scenario includes road closures from the bridge damage analysis. Each simulated scenario yields three main outputs: the traffic volume at each link for every 15 minutes of the simulation, the total travel time of each agent, and the total trip distance of each agent.

To give our simulation results some robustness to possible random variations in each run, we ran each scenario 10 times, took the average of metrics such as travel time and travel distance, and used these averages as the main results for analysis.

Damage and Traffic Loss Results

Partial verification with real-life metrics, and sensitivity to random variations

To assess the performance of our modeling framework, the Southern California Association of Governments Transportation Plan (*51*) included some metrics that are comparable to our model outputs. Some of these key metrics are:

- *Mean commute time:* SCAG lists the mean commute time—defined as the average travel time to work—as 32.1 minutes. Our input data does not have activity labels (work/non-work) but the average travel time we compute from our model is 29.4 minutes.
- *Average distance traveled:* SCAG lists the average distance traveled as 17.9 miles for work trips and 5.8 miles for non-work trips. Our model computes an overall average travel distance of 15.1 miles, which is within the SCAG range.
- *Percent of trips less than 3 miles:* SCAG states that 14.0% of work trips are less than 3 miles while 40.5% of non-work trips are less than 3 miles. Our model computes 26.1% of all trips being less than 3 miles, which is also well within the SCAG range.

From these key metrics, it was concluded that the traffic model resembles the real-life transportation scene in general despite the lack of activity labels on existing data. Availability of activity/trip purpose labels can greatly help model assessment in future studies.

Focusing on the port area, we aggregate these trip time and distance outputs for each agent to get the overall vehicle hours traveled (VHT), average travel time, and number of fulfilled & unfulfilled trips for each post-earthquake scenario relative to the base scenario, as shown in Table 9. A trip is labeled as *unfulfilled* if the vehicle is unable to travel from its origin to its destination due to damage to the road network.

Table 9. Port area measures

Scenario	Total VHT (veh-hrs)	Average Travel Time (minutes)	No. Fulfilled Trips	No. Unfulfilled Trips
Baseline (Day 0)	192.84	48.4	247,565	N/A
Day 1	179.75	51.3	210,335	37,230
Day 3	175.27	49.2	213,810	33,755
Day 7	191.49	49.1	233,785	13,780
Day 14	192.21	49.0	235,455	12,110
Day 30	192.84	48.6	238,795	8,770

Travel time variation across random seeds (base scenario) is largely from 29.32 to 29.37 minutes (around 0.05 minutes or 3 seconds as shown in Figure 49) which is much smaller than 3-min travel time increase from the base to Day 1 scenario that can be seen in Figure 54. The same trend can be observed with travel distance as can be seen in Figure 50.

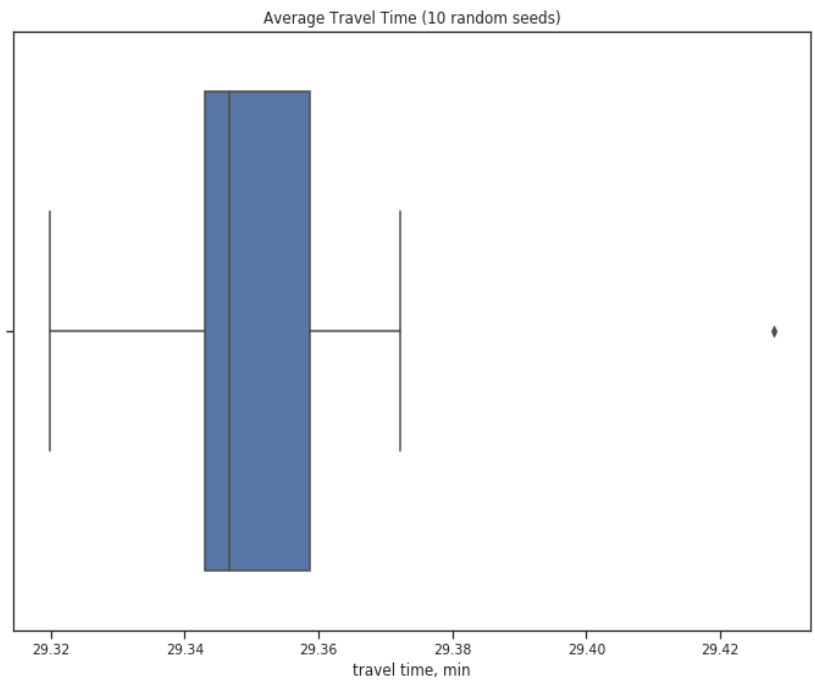

Figure 49. Travel time variation over 10 runs.

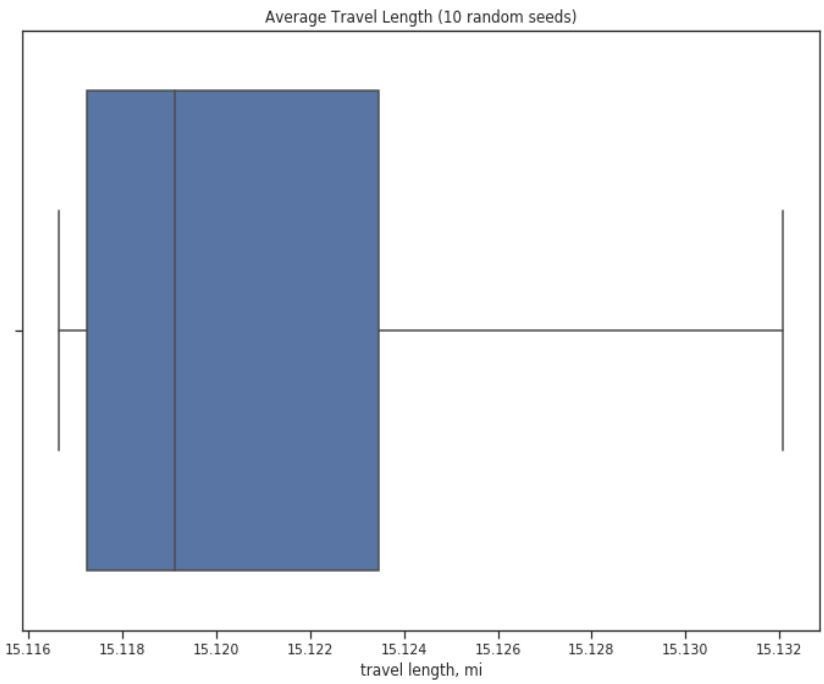

Figure 50. Travel distance variation over 10 runs.

Port area analysis

Figure 51 shows the general steps in assessing impacts to the transportation network. The primary indicator used to assess transportation network impact is the overall vehicle hours traveled (VHT). Figure 52 shows the trend in total VHT for the port area trips. There is a 10% decrease from Day 0 to Day 1, coinciding with the worst damage scenario, a small but unexpected 2.5% decrease from Day 1 to Day 3 which gives the maximum drop in VHT at 12.5%, an increase from Day 3 to Day 7 that plateaus through Day 30 at a 4% decrease relative to the base scenario.

To understand the trends in VHT, two components can be examined: the change in the number of fulfilled trips and the change in travel times. Changes in the number of fulfilled trips indicate changes in the connectivity of the road network. Figure 53 shows the trend in number of fulfilled trips starting or ending in the port area. There is a steep drop from Day 0 to Day 1 with 15% of port trips unable to be completed; this minimum coincides with the worst damage scenario right after the earthquake. There is a small increase at Day 3, and a larger increase at Day 7 that steadily increases through Day 30 when the number of unfulfilled trips is only at around 4% of total port trips. This large increase in fulfilled trips at Day 7 is due to the full reopening of a bridge that connects the eastern part of the port area to the rest of the region.

On the other hand, changes in travel times indicate a vehicle's need to detour due to closed roads. Figure 54 shows the trend of the average travel time of trips starting or ending in the port area. The average travel time increases by 6% from Day 0 to Day 1, indicating that trips still able to be completed took a longer time to do so, also coinciding again with the worst damage scenario as expected. Average travel time decreases much closer to baseline at Day 3 (with an increase of only 1.7% relative to baseline) and

steadily decreases through Day 30 when the average travel time is almost similar to that of the base scenario.

These trends are mostly intuitive except for the slight drop in the overall VHT from Day 1 to Day 3. Figure 54 and Figure 53 respectively show that the average travel time decreases at Day 3, but the number of fulfilled trips only increases incrementally. This slight drop in overall VHT therefore shows that the change in the travel time component dominates over the change in fulfilled trips. This can be attributed to the opening of a road local to the port area that helps the vehicles avoid detours while roads connecting the port area to the outside area are still closed and only start to open on Day 7. This kind of insight is one that can be made because of the resolution of the traffic simulation and its agent-based nature.

Another observation that stands out is that the increase in average travel time, at worst, is only 3 minutes. While this may seem small, it is important to note that this is delay only due to the road closures because of the earthquake. Any congestion delays already present in the baseline scenario are not separated in this paper and therefore, the actual delays will be larger than 3 minutes. Furthermore, the averaging of the changes in travel time hide a slightly disproportionate impact to certain trips. Figure 55 shows the distribution of travel times of vehicles starting or ending their trips in the port area for Day 0 and Day 1. The shape of the distributions is mostly similar, which indicates that most trip travel times stay the same. To be specific, 75% of Day 1 trips stay within 10% of their Day 0 travel time. However, over 5% (around 5000) of trips have increases of 50% of their Day 0 travel time with some even increasing by a factor of 4 or more. Again, this kind of insight can be made because of the resolution of the traffic simulation and its agent-based nature, which highlights the advantages of the adopted framework.

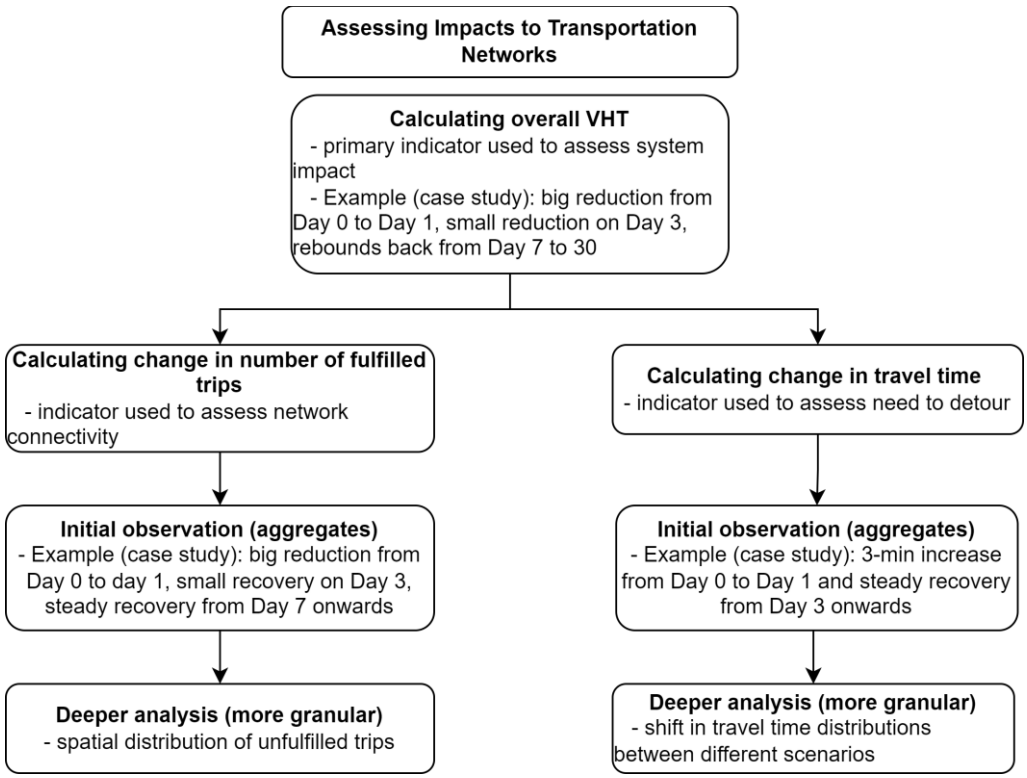

Figure 51. Assessing impacts to transportation networks.

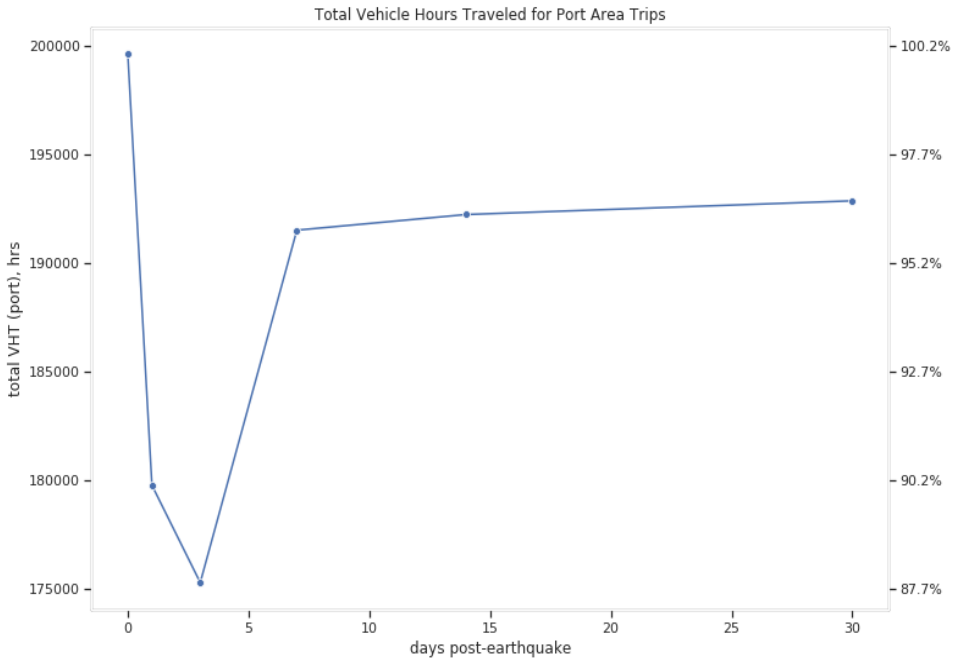

Figure 52. Change in total VHT.

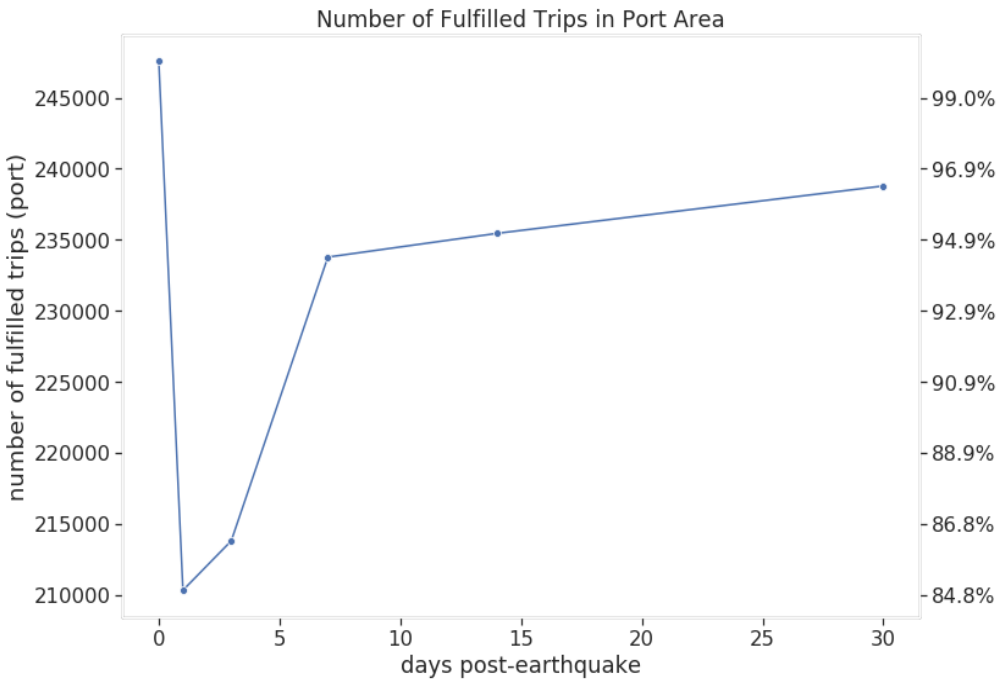

Figure 53. Change in fulfilled trips.

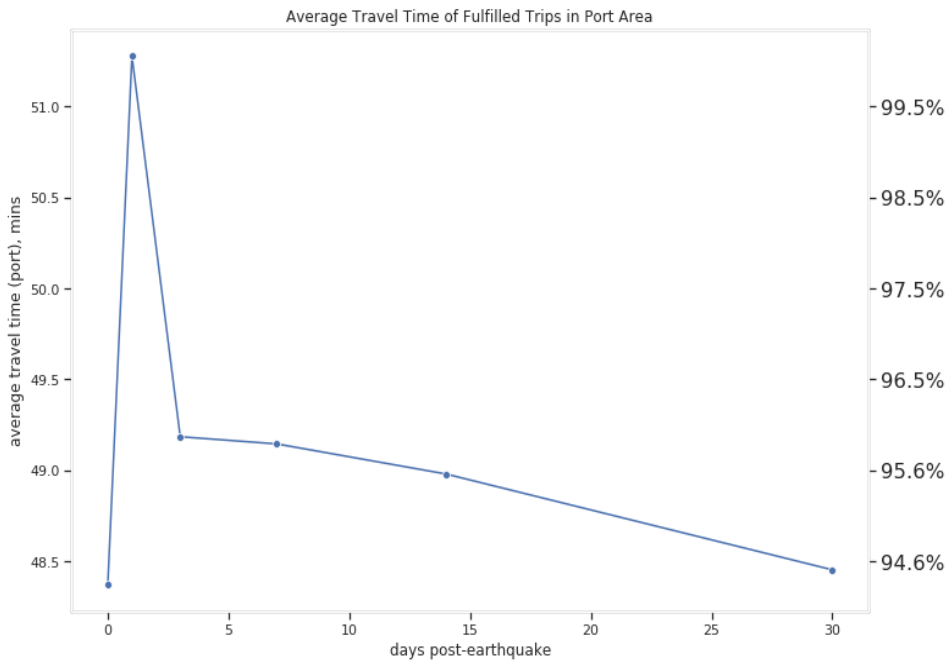

Figure 54. Change in average travel time.

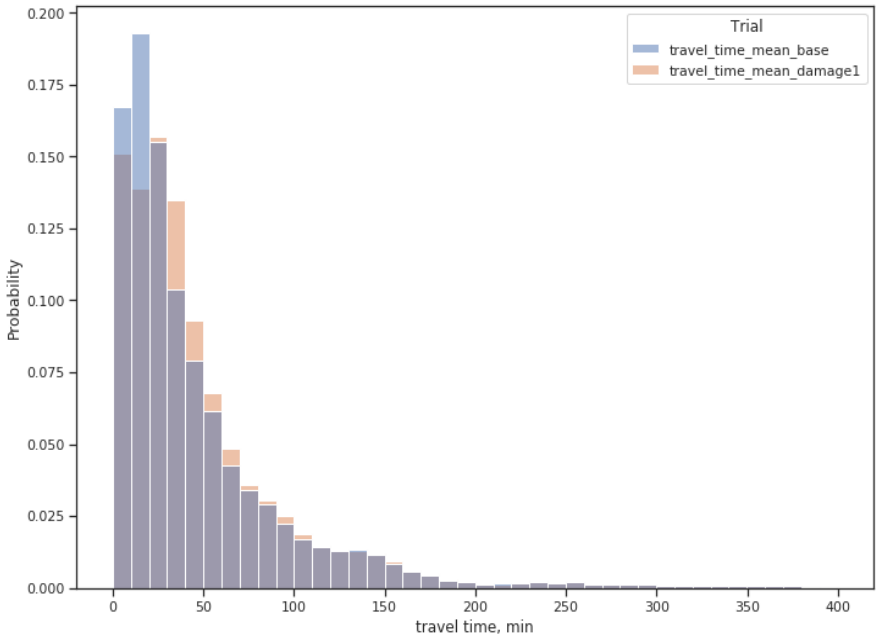

Figure 55. Travel Time Distribution.

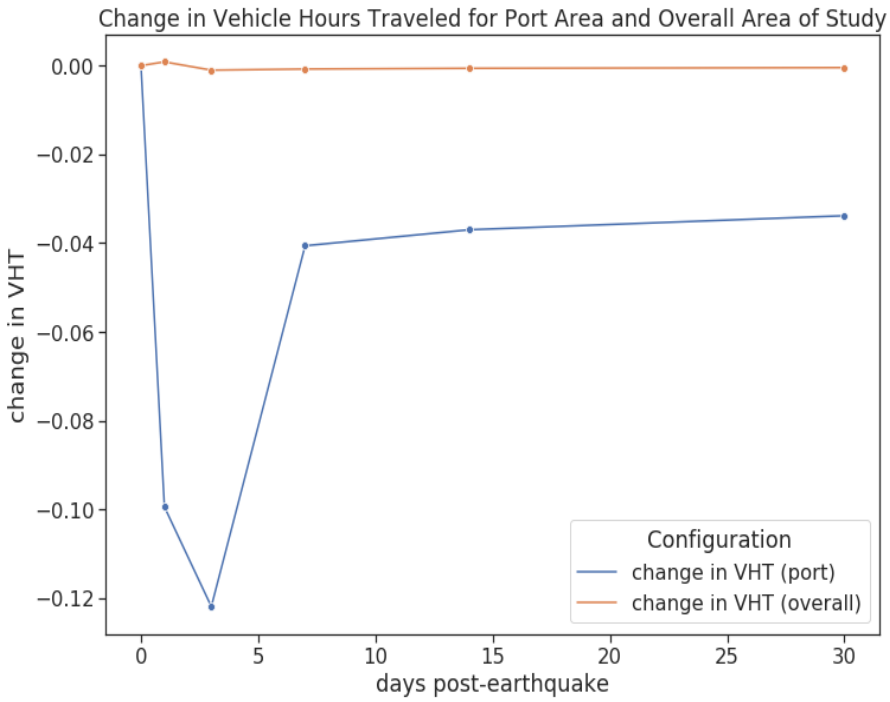

Figure 56. Change in VHT.

Minimal changes in overall VHT but sizeable decreases in port VHT

Suarez et al. (*52*) posits that the effect of hazards on VHT and VMT can be ambiguous. VHT, for example, can increase due to vehicles taking less straightforward trips on congested routes due to road closures, but can also reasonably decrease due to fewer trips. Figure 56 shows the changes in total VHT for the overall study area and the port specifically. They show that for this case study in particular, VHT changes negligibly for the overall study area over all post-earthquake scenarios. However, port VHT decrease by as much as 12%, indicating a sizeable decrease in productivity in the area. These findings align with the previous findings on changes in travel time.

Economic Impact Estimation

Using the damage maps and simulation outputs from the previous step as inputs, the direct and indirect costs caused by this hypothetical earthquake scenario are estimated. It is assumed that the roads still closed on Day 30 will be repaired by Day 60. For the SCAG area, the median household income in 2018 was 64,989 USD which translates to an α of around 31 USD per hour of delay (*53*). On the other hand, the gross regional product of California was 1,955,856 million USD in 2020 dollars and the number of labor hours was 25,101 million, which leads to a γ of 78 USD per hour per lost trip (*54*) . The resulting value indicates the estimated economic impact of the earthquake. The direct cost is calculated to be $2.30B while the indirect cost is calculated to be $768M (only $121K of which is due to traffic delays) for a total cost of $3.07B. For trips that start or end at the port area, the cost of lost demand is estimated to be at $476M, while the delays cost a minuscule $57K.

Spatially disproportionate impacts

During hazards such as floods and earthquakes, the number of agents that are able to complete their trips is always expected to decrease (*52*). This is true for our case study with there being as many as 73,845 trips that are unfulfilled in the overall SCAG area, 37,230 (or 50% of all unfulfilled trips) of which start or end in the port area. This means that as much as 62% of the total indirect cost is from the port area, showing the spatially disproportionate impact of the earthquake. Furthermore, Figure 53 shows that unfulfilled trips in the port area account for as much as 15% of all trips in the port area.

Additionally, the economic cost estimation shows that the impacts of delays are dwarfed by that of lost demand, as lost demand accounts for 99.98% of the computed indirect cost. Supporting this observation, Figure 57 shows that the economic recovery in the port area and the road restoration trend very similarly with time. Since the lost demand is a proxy indicator for the degradation of road network connectivity, this result shows that road network connectivity is the biggest issue post-earthquake as delays due to congestion are negligible relatively.

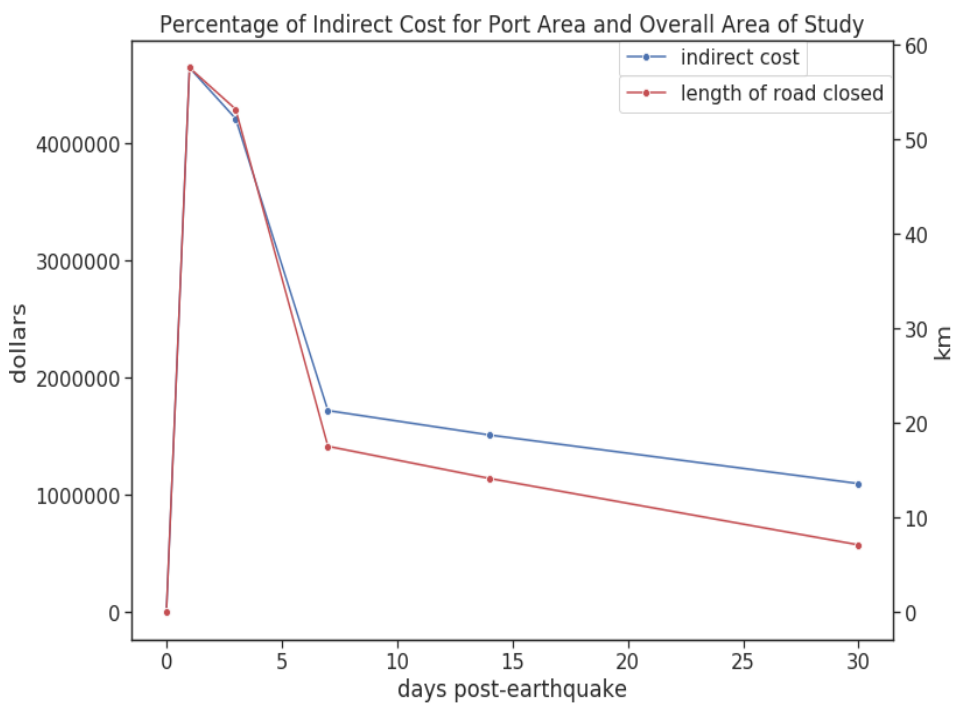

Figure 57. Indirect cost and road closures.

Local versus regional impacts

While noting that the present study focused only on losses due to disruption to the traffic network, and not even on the potential seismic damage to port structures themselves, the results suggest that damage to a generally (but not entirely) seismically resilient bridge network, which is the case for the collection of bridges surrounding the Ports of Los Angeles and Long Beach, will not produce disproportionate economic losses, even under a large nearby (M_w 7.4) seismic event. Most of the economic losses from this specific class of damage (bridge network) will be direct (due to repair/replacement of bridges, $2.30B) rather than indirect (unfulfilled trips and loss of demand, $768M). Nevertheless, the total estimated loss is significant

($3.07B) and will likely contribute significantly to the regional losses. On the other hand, it is unlikely that Port-related losses ($768M) will dominate the regional losses, because the predicted losses here are significantly smaller than the overall economic impact estimates for historical seismic events like a gross regional product (GRP) reduction of $75B and property damage of $31B for the 1994 Northridge earthquake or the $15B rebuild costs and $25B property damage for the 2010 and 2011 series of rthquakes in Canterbury, New Zealand (*55*). Moreover, Detweiler and Wein (*55*) posit that individual GDP losses from utilities like water, power, or telecommunication outages do not exceed $900M, which, in general terms, corroborates this study's findings.

It is also reasonable to conclude that the potential impact of local bridge closures to California's overall economy will be minimal. In 2020, California's gross domestic product (GDP) was estimated to be at $3.16T, with the six-county SCAG region's collective GDP comprising $1.19T of this amount (*56*). Overall, this shows that the estimated economic impact is only 0.26% of SCAG's total GDP. Furthermore, given that there are other west-coast ports (Oakland, Seattle), it is possible that some or all of the POLA/POLB traffic might be diverted there, at least during the recovery process, thereby limiting the overall nation-wide impact. Of course, such initially short-term changes may lead to long-term supply-chain realignments, adversely affecting Southern California's economy, but analyses long-term effects are outside of the scope of the present study.

It should be noted carefully, however, that the present study did not consider the direct seismic damage to port structures (wharves, cranes, container yards, etc.) due to ground shaking, or more importantly, the tsunami/inundation hazard, which could potentially close the entire port indefinitely. Impacts to the ports' productivity can also lead to cascading economic impacts that are more challenging to quantify. In the past year, the COVID-19 pandemic and a subsequent change in consumer behavior led to congestion in the ports and supply chain shortage(*57–59*)—the full impacts of which are yet to be studied.

Summary, Conclusions, and Suggested Future Work

This study presented a highly granular synthesis framework to quantify the resilience of transportation networks to hazards such as earthquakes, including seismic loss and recovery. The framework starts with the characterization of the hazard and determining the probable seismic demands. Second is the assessment of damage to the bridge infrastructure, which is carried out by individually modeling the bridges and simulating their responses in order to obtain seismic fragility curves. These seismic fragilities can then be used to rapidly estimate damage under scenario (the approach taken here) or real-life events. The resulting estimated damage (i.e., functionality losses) are then used as inputs to a transportation network analysis, which runs semi-dynamic traffic assignment on the network over a 24-hour period under the base scenario pre-earthquake and the modified networks post-earthquake. The output road usage and individual agent travel times are then used for estimating the economic impact of the earthquake to the transportation network through direct costs (repair) and indirect costs (delays, loss of connectivity).

The case study on two neighboring Southern California ports (Los Angeles and Long Beach) produced results that are in general alignment with prior simulation-based studies and event-based observations on seismic damage and economic impact. These results indicated that the economic impacts of the damage to the transportation network will be localized, and the overall losses will be dominated by direct losses (repairing or replacing the damaged bridges). This is primarily because the traffic will still be able to flow in and out of the ports (albeit at a significantly diminished level initially), because not all of the connecting bridges will collapse or otherwise lose their functionality.

To improve this resilience assessment and recovery prediction framework, considering different modes of transport and having more information on a vehicle's activity (e.g. work, leisure, etc.) can help in better quantifying the economic cost of each trip and the overall economic impact to the transportation network.

Regarding the economic loss analysis, it appears important to simultaneously assess the seismic damage to the port structures themselves, which will reduce the ports' functionality. In that case, the damage to the bridge network might play an additional negative (potentially disproportional) effect, by delaying the repair operations at the ports. Another important study that could be undertaken appears to be tsunami-related damages to the port structures. However, the current economic analysis and loss/cost estimation as it stands should be useful to policy- and decision-makers who work best with having concrete figures as evidence in making short- or long-term decisions on these critical infrastructures.

References

1. Petersen, M. D., A. M. Shumway, P. M. Powers, C. S. Mueller, M. P. Moschetti, A. D. Frankel, S. Rezaeian, D. E. McNamara, N. Luco, O. S. Boyd, K. S. Rukstales, K. S. Jaiswal, E. M. Thompson, S. M. Hoover, B. S. Clayton, E. H. Field, and Y. Zeng. The 2018 Update of the US National Seismic Hazard Model: Overview of Model and Implications. *Earthquake Spectra*, Vol. 36, No. 1, 2020, pp. 5–41. https://doi.org/10.1177/8755293019878199.

2. Ancheta, T. D., R. B. Darragh, J. P. Stewart, E. Seyhan, W. J. Silva, B. S. J. Chiou, K. E. Wooddell, R. W. Graves, A. R. Kottke, D. M. Boore, T. Kishida, and J. L. Donahue. *PEER NGA-West2 Database*. Berkeley, CA, 2013.

3. Moehle, J., and G. G. Deierlein. A Framework Methodology for Performance-Based Earthquake Engineering. *Proceedings of the 13th World Conference on Earthquake Engineering*, No. 679, 2004, pp. 3812–3814. https://doi.org/10.1061/9780784412121.173.

4. Kircher, C. A., R. V. Whitman, and W. T. Holmes. HAZUS Earthquake Loss Estimation Methods. *Natural Hazards Review*, Vol. 7, No. 2, 2006, pp. 45–59. https://doi.org/10.1061/(ASCE)1527-6988(2006)7:2(45).

5. Isbiliroglu, Y., R. Taborda, and J. Bielak. Coupled Soil-Structure Interaction Effects of Building Clusters during Earthquakes. *Earthquake Spectra*, Vol. 31, No. 1, 2015, pp. 463–500. https://doi.org/10.1193/102412EQS315M.

6. Kim, Y. C., A. Yoshida, and Y. Tamura. Influence of Surrounding Buildings on Wind Loads Acting on Low-Rise Building. *Journal of Structural Engineering*, Vol. 139, No. 2, 2013, pp. 275–283. https://doi.org/10.1061/(ASCE)ST.1943-541X.0000625.

7. Wanik, D. W., E. N. Anagnostou, M. Astitha, B. M. Hartman, G. M. Lackmann, J. Yang, D. Cerrai, J. He, and M. E. B. Frediani. A Case Study on Power Outage Impacts from Future Hurricane Sandy Scenarios. *Journal of Applied Meteorology and Climatology*, Vol. 57, No. 1, 2018, pp. 51–79. https://doi.org/10.1175/JAMC-D-16-0408.1.

8. Campbell, R. J. *Weather-Related Power Outages and Electric System Resiliency*. Washington D.C., 2012.

9. Holzer, T. L. The 1995 Hanshin-Awaji (Kobe), Japan, Earthquake. GSA TODAY, 5, 8, , 1995, pp. 154–167.

10. Chung, R. *January 17, 1995 Hyogoken-Nanbu (Kobe) Earthquake: Performance of Structures, Lifelines, and Fire Protection Systems (NIST SP 901)*. Gaithersburg, MD, 1996.

11. Dolfman, M. L., S. F. Wasser, and B. Bergman. The Effects of Hurricane Katrina on the New Orleans Economy. *Monthly Labor Review*, Vol. 130, No. 3, 2007, pp. 3–18.

12. Wildasin, D. E. *Disasters: Issues for State and Federal Government Finances*. Publication 2006–07. Lexington, KY, 2006.

13. Federal Emergency Management Agency. *Summary Report on Building Performance: Hurricane*

Katrina 2005. Washington D.C., 2006.

14. Rathje, E. M., C. Dawson, J. E. Padgett, J.-P. Pinelli, D. Stanzione, A. Adair, P. Arduino, S. J. Brandenberg, T. Cockerill, C. Dey, M. Esteva, F. L. Haan Jr, M. Hanlon, A. Kareem, L. Lowes, S. Mock, and G. Mosqueda. DesignSafe: New Cyberinfrastructure for Natural Hazards Engineering. *Natural Hazards Review*, Vol. 18, No. 3, 2017, p. 06017001. https://doi.org/10.1061/(ASCE)NH.1527-6996.0000246.

15. Federal Emergency Management Agency. Hazus–MH 2.1 Earthquake Model Technical Manual.

16. Wald, D. J., K. S. Jaiswal, D. B. Bausch, and M. G. Hearne. *PAGER — Rapid Assessment of an Earthquake's Impact*. Golden, CO, 2010.

17. Mangalathu, S. *Performance Based Grouping and Fragility Analysis of Box-Girder Bridges in California*. Georgia Institute of Technology, 2017.

18. McKenna, F. OpenSees: A Framework for Earthquake Engineering Simulation. *Computing in Science and Engineering*, Vol. 13, No. 4, 2011, pp. 58–66. https://doi.org/10.1109/MCSE.2011.66.

19. Mander, J. B., M. J. N. Priestley, and R. Park. Theoretical Stress-Strain Model for Confined Concrete. *Journal of Structural Engineering*, Vol. 114, No. 8, 1988, pp. 1804–1826. https://doi.org/10.1061/(ASCE)0733-9445(1988)114:8(1804).

20. Popovics, S. A Numerical Approach to the Complete Stress-Strain Curve of Concrete. *Cement and Concrete Research*, Vol. 3, No. 5, 1973, pp. 583–599. https://doi.org/10.1016/0008-8846(73)90096-3.

21. State of California Department of Transportation. *Caltrans Seismic Design Criteria Version 2.0*. Caltrans, Sacramento, CA, 2019.

22. Chang, G. A., and J. B. Mander. Seismic Energy Based Fatigue Damage Analysis of Bridge Columns: Part 1--Evaluation of Seismic Capacity. *NCEER Technical Rep. No. NCEER-94*, Vol. 6, 1994.

23. Neuenhofer, A., and F. C. Filippou. Evaluation of Nonlinear Frame Finite-Element Models. *Journal of Structural Engineering*, Vol. 123, No. 7, 1997, pp. 958–966. https://doi.org/10.1061/(asce)0733-9445(1997)123:7(958).

24. Hildebrand, Francis, B. *Introduction to Numerical Analysis*. Dover Publications, New York, 2013.

25. Aviram, A., K. R. Mackie, and B. Stojadinovic. *Guidelines of Nonlinear Analysis of Bridge Structures in California*. Berkeley, CA, 2008.

26. Highway Subcommittee on Bridges and Structures. *AASHTO LRFD Bridge Design Specifications*. American Association of State Highway and Transportation Officials, Washington, DC, 2014.

27. Kaviani, P., F. Zareian, and E. Taciroglu. *Performance-Based Seismic Assessment of Skewed Bridges*. Berkeley, CA, 2014.

28. Muthukumar, S. *A Contact Element Approach with Hysteresis Damping for the Analysis and Design*

of Pounding in Bridges. Georgia Institute of Technology, 2003.

29. Hube, M. A., and K. M. Mosalam. *Experimental and Computational Evaluation of Current and Innovative In-Span Hinge Details in Reinforced Concrete Box-Girder Bridges - Part 1: Experimental Findings and Pre-Test Analysis*. Berkeley, CA, 2008.

30. Megally, S., P. Silva, and F. Seible. *Technical Report SSRP 2001/23: Seismic Response of Sacrificial Shear Keys in Bridge Abutments*. San Diego, CA, 2001.

31. Priestley, M. J. N., F. Seible, and G. M. Calvi. *Seismic Design and Retrofit of Bridges*. John Wiley and Sons, New York, NY, 1996.

32. Ramanathan, K. N. *Next Generation Seismic Fragility Curves for California Bridges Incorporating the Evolution in Seismic Design Philosophy*. Georgia Institute of Technology, 2012.

33. Khalili-Tehrani, P., A. Shamsabadi, J. P. Stewart, and E. Taciroglu. Backbone Curves with Physical Parameters for Passive Lateral Response of Homogeneous Abutment Backfills. *Bulletin of Earthquake Engineering*, Vol. 14, No. 11, 2016, pp. 3003–3023. https://doi.org/10.1007/s10518-016-9934-3.

34. Inc., E. M. *Field Investigation Report for Abutment Backfill Characterization*. Los Jolla, CA, 2005.

35. Stewart, J. P., E. Taciroglu, J. W. Wallace, E. R. Ahlberg, A. Lemnitzer, C. Rha, P. K. Tehrani, S. Keowen, R. L. Nighbor, and A. Salamanca. *Full Scale Cyclic Testing of Foundation Support Systems for Highway Bridges. Part II: Abutment Backwalls*. Los Angeles, CA, 2007.

36. Padgett, J. E., B. G. Nielson, and R. DesRoches. Selection of Optimal Intensity Measures in Probabilistic Seismic Demand Models of Highway Bridge Portfolios. *Earthquake Engineering \& Structural Dynamics*, Vol. 37, No. 5, 2008, pp. 711–725.

37. FHWA. *Recording and Coding Guide for the Structure Inventory and Appraisal of the Nation's Bridges*. Washington, D.C., 1995.

38. OpenStreetMap contributors. Planet Dump Retrieved from Https://Planet.Osm.Org .

39. US Census Bureau. Tiger/Line Shapefiles. *Census.gov*. https://www.census.gov/geographies/mapping-files/time-series/geo/tiger-line-file.html.

40. Chen, L.-C., G. Papandreou, F. Schroff, and H. Adam. Rethinking Atrous Convolution for Semantic Image Segmentation. *CoRR*, Vol. abs/1706.05587, 2017.

41. Zhou, Y., H. Qi, and Y. Ma. End-to-End Wireframe Parsing. 2019.

42. Vasconcelos, F., J. P. Barreto, and E. Boyer. Automatic Camera Calibration Using Multiple Sets of Pairwise Correspondences. *IEEE Transactions on Pattern Analysis and Machine Intelligence*, Vol. 40, No. 4, 2018, pp. 791–803. https://doi.org/10.1109/TPAMI.2017.2699648.

43. Ramanathan, K., J. E. Padgett, and R. DesRoches. Temporal Evolution of Seismic Fragility Curves for Concrete Box-Girder Bridges in California. *Engineering Structures*, Vol. 97, 2015, pp. 29–46.

https://doi.org/10.1016/J.ENGSTRUCT.2015.03.069.

44. Chan, C., A. Kuncheria, B. Zhao, T. Cabannes, A. Keimer, B. Wang, A. Bayen, and J. Macfarlane. Quasi-Dynamic Traffic Assignment Using High Performance Computing. 2021. https://doi.org/10.48550/ARXIV.2104.12911.

45. Boeing, G. OSMnx: New Methods for Acquiring, Constructing, Analyzing, and Visualizing Complex Street Networks. *Computers, Environment and Urban Systems*, Vol. 65, 2017, pp. 126–139.

46. USBPC. *United States Bureau of Public Roads Traffic Assignment Manual for Application with a Large, High-Speed Computer*. 1964.

47. Bhattacharjee, G., and J. W. Baker. Using Global Variance-Based Sensitivity Analysis to Prioritise Bridge Retrofits in a Regional Road Network Subject to Seismic Hazard. *Structure and Infrastructure Engineering*, 2021, pp. 1–14.

48. Small, P., D. Gill, P. J. Maechling, R. Taborda, S. Callaghan, T. H. Jordan, K. B. Olsen, G. P. Ely, and C. Goulet. The SCEC Unified Community Velocity Model Software Framework. *Seismological Research Letters*, Vol. 88, No. 6, 2017, pp. 1539–1552. https://doi.org/10.1785/0220170082.

49. Khademi, N., B. Balaei, M. Shahri, M. Mirzaei, B. Sarrafi, M. Zahabiun, and A. S. Mohaymany. Transportation Network Vulnerability Analysis for the Case of a Catastrophic Earthquake. *International journal of disaster risk reduction*, Vol. 12, 2015, pp. 234–254.

50. Foti, F., P. Waddell, and D. Luxen. A Generalized Computational Framework for Accessibility: From the Pedestrian to the Metropolitan Scale. 2012.

51. Southern California Association of Governments. *Connect SoCal - The 2020-2045 Regional Transportation Plan/Sustainable Communities Strategy*. 2020.

52. Suarez, P., W. Anderson, V. Mahal, and T. R. Lakshmanan. Impacts of Flooding and Climate Change on Urban Transportation: A Systemwide Performance Assessment of the Boston Metro Area. *Transportation Research Part D: transport and environment*, Vol. 10, No. 3, 2005, pp. 231–244.

53. Southern California Association of Governments. Profile of the City of Anaheim.

54. Pabilonia, S., M. Jadoo, B. Khandrika, J. Price, and J. Mildenberger. {BLS} Publishes Experimental State-Level Labor Productivity Measures. *Monthly Labor Review*, 2019. https://doi.org/10.21916/mlr.2019.12.

55. Detweiler, S. T., and A. M. Wein. *The HayWired Earthquake Scenario-Societal Consequences*. 2019.

56. US Bureau of Economic Analysis. Gross Domestic Product by County, 2019.

57. Isidore, C. Everything You're Waiting for Is in These Containers. *CNN*. https://www.cnn.com/2021/10/20/business/la-long-beach-port-congestion-problem-national-impact/index.html.

58. The White House. Recent Progress and Actions on Port Congestion. *whitehouse.gov*.

https://www.whitehouse.gov/briefing-room/blog/2021/11/10/recent-progress-and-actions-on-port-congestion/.

59. Dean, S. Is the Ports Logjam Really Getting Better? The Numbers Don't Tell the Whole Story. *Los Angeles Times*. https://www.latimes.com/business/story/2021-12-03/officials-say-the-ports-logjam-is-easing-but-numbers-dont-tell-the-whole-story.

Data Management Plan

Products of Research

This research produces seismic fragility functions for 1000 bridges around the Ports of Los Angeles and Long Beach.

Data Format and Content

The seismic fragility functions are provided in a CSV file that has 10 data columns, given in the following order:

bridge_latitude, bridge_longitude, minor_damage_median, minor_damage_dispersion, moderate_damage_median, moderate_damage_dispersion, extensive_damage_media, extensive_damage_dispersion, complete_damage_median, complete_damage_dispersion

Data Access and Sharing

The data file is available to the general public at the DesignSafe-CI Data Depot, which is maintained by UT Austin's Texas Advanced Computing Center (TACC). The file is accessible through the following URL:

https://www.designsafe-ci.org/data/browser/projects/243694523301040621-242ac11a-0001-012/

Reuse and Redistribution

The resulting data can be freely used and redistributed. The authors of this study assume no responsibility for the use and interpretation of this data, which has been produced for academic research purposes, but not for actual risk assessment, management, or policy decisions.